AFRL-AFOSR-VA-TR-2017-0054

Energy Transformation, Transfer, and Release Dynamics in High-Speed Turbulent Flows

Paul Dimotakis
CALIFORNIA INSTITUTE OF TECHNOLOGY
1200 E. CALIFORNIA BLDV
PASADENA, CA 91125

03/19/2017
Final Report

Air Force Research Laboratory
AF Office Of Scientific Research (AFOSR)/RTA1

REPORT DOCUMENTATION PAGE

Form Approved
OMB No. 0704-0188

1. REPORT DATE *(DD-MM-YYYY)* 01-03-2017	**2. REPORT TYPE** Final technical	**3. DATES COVERED** *(From - To)* 30-09-2012 - 30-11-2016

4. TITLE AND SUBTITLE

Energy transformation, transfer, and release dynamics in high-speed turbulent flows

5a. CONTRACT NUMBER

5b. GRANT NUMBER
FA9550-12-1-0461

5c. PROGRAM ELEMENT NUMBER

6. AUTHOR(S)

Paul E. Dimotakis and Graham V. Candler

5d. PROJECT NUMBER

5e. TASK NUMBER

5f. WORK UNIT NUMBER

7. PERFORMING ORGANIZATION NAME(S) AND ADDRESS(ES)

Graduate Aerospace Laboratories
California Institute of Technology
1200 E. California Blvd.
Pasadena, CA 91125

8. PERFORMING ORGANIZATION REPORT NUMBER

9. SPONSORING / MONITORING AGENCY NAME(S) AND ADDRESS(ES)

Air Force Office of Scientific Research
875 North Randolph Street, Suite 325, Room 3112,
Arlington, VA 22203-1768

10. SPONSOR/MONITOR'S ACRONYM(S)

11. SPONSOR/MONITOR'S REPORT NUMBER(S)

12. DISTRIBUTION / AVAILABILITY STATEMENT

DISTRIBUTION A: Distribution approved for public release.

13. SUPPLEMENTARY NOTES

14. ABSTRACT

Delay length for chemical-reaction initiation downstream of jet-injection was attributed to turbulent mixing and not chemical kinetics, for flows investigated. Inclined-jet injection dramatically decreases freestream-flow disturbances, relative to normal-jet injection, but increases ignition distance. This penalty may be acceptable considering the lower total-pressure losses than for normal injection. New experimental techniques developed allowed non-intrusive measurement of convecting velocity fields in supersonic flows and used for validation of LES of jet-injection flow in a supersonic stream. Small-scale experiments revealed 3D behavior of scalar mixing. In DNS, the turbulent fluid-mixing behavior of fluids with variable density revealed new scaling, providing guidance for subgrid-scale modeling of variable-density flows. A new subgrid-scale (SGS) combustion model (EVM) was developed for distributed-reaction zone (DRZ) environments allowing efficient computation of turbulent combustion, extending to hydrocarbon combustion. Integrated in a LES of turbulent combustion of a hydrogen jet in supersonic air crossflow it captured many important flow features. Unphysical scalar excursions in finite-difference LES modeling were traced to dispersion errors of finite-difference operators. Many presentations, conference papers, and publications derived from this effort, as listed and discussed in the report.

15. SUBJECT TERMS

16. SECURITY CLASSIFICATION OF:			**17. LIMITATION OF ABSTRACT**	**18. NUMBER OF PAGES**	**19a. NAME OF RESPONSIBLE PERSON** Dr. Chiping Li, AFOSR/RTE
a. REPORT U	**b. ABSTRACT** U	**c. THIS PAGE** U	SAR	46	**19b. TELEPHONE NUMBER** *(include area code)* (703) 696-8574

Standard Form 298 (Rev. 8-98)
Prescribed by ANSI Std. Z39.18

[This page intentionally left blank.]

GRADUATE AEROSPACE LABORATORIES
CALIFORNIA INSTITUTE OF TECHNOLOGY
Pasadena, California 91125

ENERGY TRANSFORMATION, TRANSFER, AND RELEASE DYNAMICS IN HIGH-SPEED TURBULENT FLOWS

Paul E. Dimotakis (PI), California Institute of Technology
Graham V. Candler (Co-PI), University of Minnesota

Air Force Office of Scientific Research, Grant FA9550-12-1-0461
Program Manager: Dr. Chiping Li

Final Research Report for the period
30 September 2012 to 30 November 2016

28 February 2017
(Corrected, 1 March 2017)

[This page intentionally left blank].

1. Introduction

This is the final report documenting accomplishments and progress as a result of research performed under the AFOSR Grant FA9550-12-1-0461, over a period of 50 months, spanning from 30 September 2012 through 30 November 2016, following previous and initial guidance by Dr. Julian Tishkoff and subsequently by Dr. Chiping Li serving as program managers. The research and work represented a closely knit collaborative effort between the California Institute of Technology, with Prof. Paul E. Dimotakis serving as Principal Investigator (PI), and the University of Minnesota, with Prof. Graham V. Candler serving as Co-Principal Investigator (Co-PI).

The research effort focused on high-speed air-breathing propulsion and turbulent-combustion flows and environments, and was comprised of several parts in which significant accomplishments were made:

1. An experimental effort focusing on investigations in:
   a. supersonic-flow turbulent mixing, in both chemically reacting and non-reacting flow, as well as
   b. small-scale fully resolved scalar mixing experiments aimed at providing guidance to and validation of subgrid-scale model of scalar transport and mixing.
2. An equipment and instrumentation effort comprised of experimental technology and high-speed data-acquisition developments, as well as modeling and simulation advances that permitted new validation approaches of large-eddy simulation (LES) numerical modeling based on detailed forward-modeling of shadowgraph-schlieren optical imaging.
3. A theoretical and numerical-simulation effort focused on subgrid-scale (SGS) model and LES developments:
   a. non-reacting variable-density compressible and incompressible flows;
   b. subgrid-scale modeling of turbulent combustion, extending to hydrocarbon combustion, and yielding a new framework for such modeling dubbed the evolution-variable manifold (EVM) method;
   c. development of numerical flux functions and implementation of the evolution-variable manifold (EVM) approach in the University of Minnesota US3D computational fluid dynamics code;
   d. Simulations of low-speed and supersonic Caltech hydrogen-fluorine reacting mixing-layer experiments
   e. Development of a novel SGS modeling approach for LES modeling of compressible and variable-density flows
4. Theoretical and numerical investigations of unphysical scalar excursions that arise as the result of dispersive errors encountered in the transport of passive and active scalars in finite-difference numerical-simulation schemes, and preliminary investigations of mitigation measures for both passive and active scalars.

5. Large-scale direct numerical simulation (DNS) modeling of turbulent flows that mix two fluids spanning density ratios, $R = \rho_1/\rho_2$, in the range of $1.005 \leq R \leq 10$, based on spectral numerical methods that are free of the dispersive errors outlined under Item 4, above. Turbulent hydrocarbon combustion, for example, entails flow spanning density variations of order $R = \rho_{\mathrm{unburnt}}/\rho_{\mathrm{burnt}} \simeq 7$ for reactions between species starting at normal temperatures and pressures. These investigations aim to probe and understand dynamics such as baroclinic torques not encountered in (near-)uniform-density flows.

To date, this work has been documented in papers in various stages, i.e., published, submitted, or in preparation at this writing, as well as in topical conference presentations and papers.

Research completed under this project enables several advances. Importantly, efficient LES modeling of complex-geometry high-speed-propulsion flow paths with turbulent combustion in scramjet-type combustors is now possible. The EVM-LES approach could in the future be extended to long-chain hydrocarbon fuels using recent advances in the modeling of fuel breakdown and pyrolysis, followed by oxidation of short-chain species. Crucially, the present research developed an accurate approach for correctly linking multi-dimensional tabulated EVM data to thermodynamic processes that must be correctly captured by and represented in the numerical method.

The effort benefitted from progress under previous support by AFOSR Grant FA9550-07-1-0091 and the AFOSR DURIP Grant FA9550-10-1-0553, as well as use of equipment and instrumentation previously developed under a NSF Major Research Instrumentation Grant EIA-0079871. More recently and concurrently, it benefitted by support under the DOE Research Grant Award DE-NA0002382 that continues at this writing and support for I. Gat at Caltech by the NSF Graduate Research Fellowship Program Grant Award DGE-1144469. Further support was provided by the Caltech academic program, and the Caltech Northrop Chair in Aeronautics, as well as through the McKnight Presidential Professorship at the University of Minnesota.

Computing support was also provided by the Blue Waters sustained-petascale computing project, supported by NSF Awards OCI-0725070 and ACI-1238993, and the state of Illinois. Blue Waters is a joint effort of the University of Illinois at Urbana-Champaign and its National Center for Supercomputing Applications. Simulations performed on Blue Waters were under NSF PRAC award number ACI-1440083. Computations were also performed on the Caltech Zwicky computer cluster, supported by NSF MRI-R2 Award PHY-0060291 and by the Sherman Fairchild Foundation. The work was also supported by the Cray Trinity system of the Alliance for Computing at Extreme Scale (ACES), a partnership between Los Alamos National Laboratory and Sandia National Laboratories for the U.S. Dept. of Energy's NNSA. Data storage and visualization were facilitated by a computer cluster integrated by Daniel Lang and developed through support by NSF MRI Grant EIA-0079871, AFOSR DURIP Grant FA9550-10-1-0553, and support by the AFOSR and DOE grants mentioned above. Computational support was also provided by the University of Minnesota Supercomputing Institute, the University of Minnesota Aerospace Engineering & Mechanics computer clusters, and the DoD HPC systems through the

AFOSR grant support. We would finally like to acknowledge discussions with Profs. Dan Meiron and Dale Pullin, and a collaboration in the computations with Prof. Christian Ott.

The research teams comprised of faculty, students, post-docs, and other researchers and collaborators are grateful to the AFOSR and other support provided that enabled the important progress we report on below.

[This page intentionally left blank.]

2. Research and progress under this grant

Research, accomplishments, and progress realized under this Grant, as outlined in the Introduction, are documented below.

2.1 Experimental effort

This section summarizes the experimental effort performed under this Grant and documents its results.

2.1.1 Experiments in supersonic flow and mixing

Several experiments were undertaken in supersonic flow investigating the behavior and of both reacting and non-reacting flows. These were primarily focused on transverse-jet injection in supersonic cross-flows; a rich flow environment relevant to scramjet propulsion that encompasses many of the dynamics investigated separately, either experimentally or computationally, as discussed below. See Figure 1.

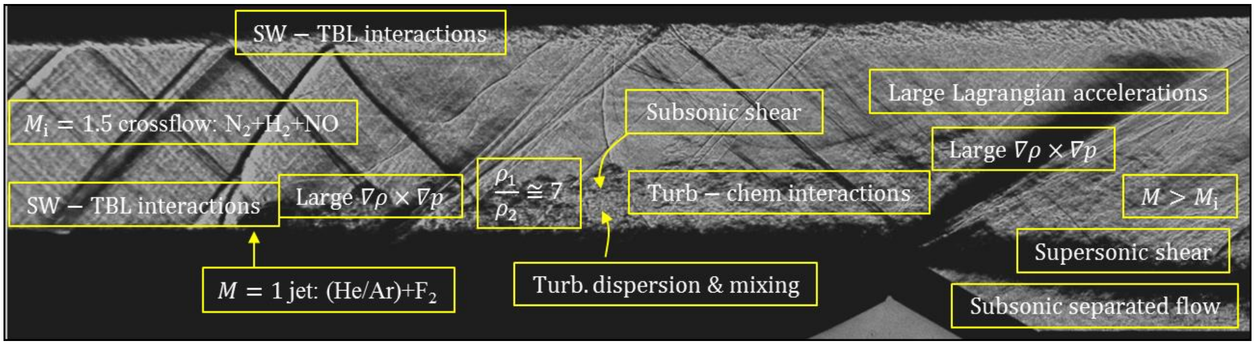

Figure 1. Transverse-jet injection in supersonic crossflow with an inflow Mach number of $M_\mathrm{i} = 1.5$.

These experiments necessitated modifications to the test-section to enable a modular arrangement for interchangeable blocks for jet injection at 90$^\mathrm{o}$, or inclined at 30$^\mathrm{o}$, with round jets of different diameters, specially designed jet inlets to avoid complications from sharp inlet edges, diamond jet arrays, or single jets, or jets in combination (Cymbalist 2016). They also required the development of new experimental technologies and instrumentation that were undertaken under support of this grant as well as support from the AFOSR DURIP Grant FA9550-10-1-0553 and developments under previous AFOSR and NSF support, as outlined in the Introduction.

Optical diagnostics employed combined shadowgraph-schlieren techniques with high-speed/-resolution digital-image recording, with concurrent chemiluminescence imaging recorded on a gated image-intensified camera. These diagnostics exploited counter-propagating optical beams with a west-to-east propagation for the shadowgraph-schlieren data and a west-to-east propagation for the chemiluminescent data, further separated from each other exploiting optical wavelength differences using dichroic optics. A schematic diagram of the combined optical system is depicted in Figure 2 from Cymbalist (2016).

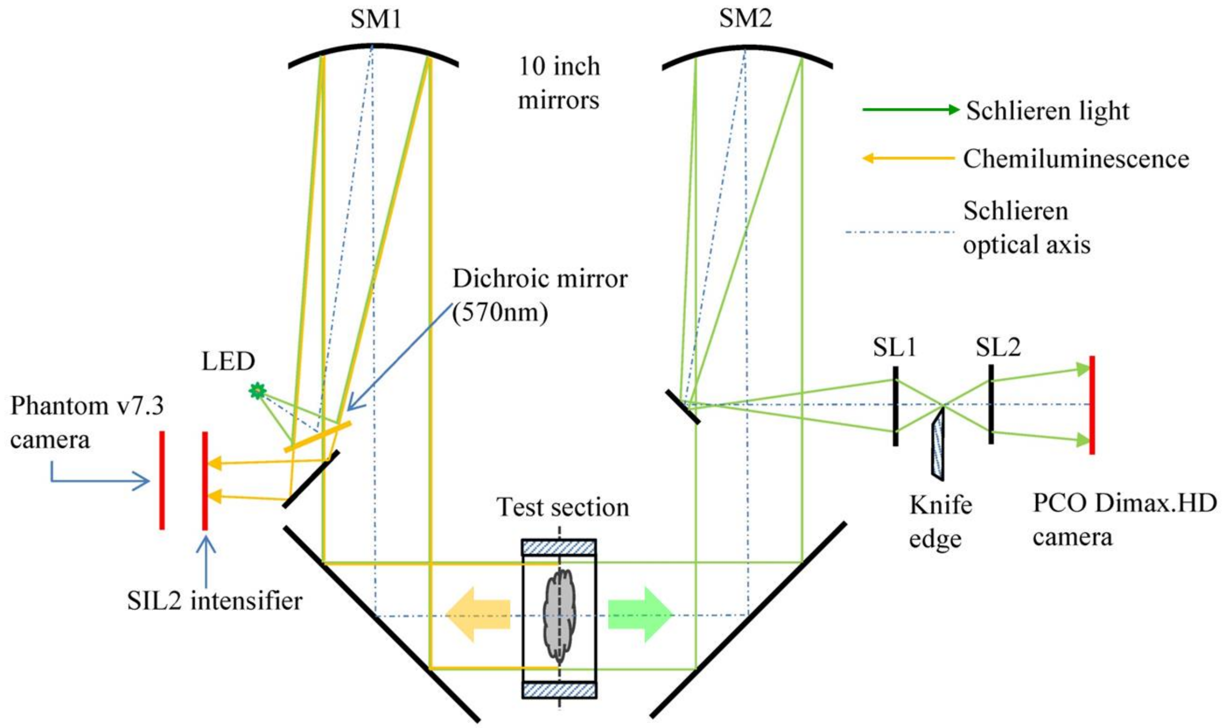

Figure 2. Schematic of combined shadowgraph-schlieren and chemiluminescence optical diagnostic system (Cymbalist 2016, Fig. 2.4).

Images were co-registered on the computer exploiting fiducials in the images and could either be superimposed or processed separately to yield instantaneous (μs) density fields, or chemiluminescence fields, as illustrated in the transverse-jet injection in a supersonic ($M_{\mathrm{i}} = 1.5$) crossflow in Figure 3. The Mach-wave, bow-shock, acoustic-wave system, and chemiluminescence intensity distribution are discernible in that figure.

Three distinct regions are discernible in the bottom annotated chemiluminescence frame-averaged image, with ℓ_{m} a spatial-delay length. Also interesting in Figure 3 is the near-wall reaction zone that can be seen to even extend slightly upstream of the jet, marking the horseshoe recirculation zone around the jet and the long residence times giving reactions the opportunity to take place in that region.

Chemical-kinetics as well as mixing scaling analyses were explored as causes to investigate the dependence of the delay length as this is an important parameter in scramjet combustion and propulsion.

The hydrogen-fluorine chemical system is relatively simple and kinetically fast, even at low reactant concentrations, so it was possible to exclude kinetics by performing kinetics-delay estimates as the cause for this spatial delay. This was further confirmed by changing kinetics rates experimentally by increasing reactant concentrations, which had a very small effect.

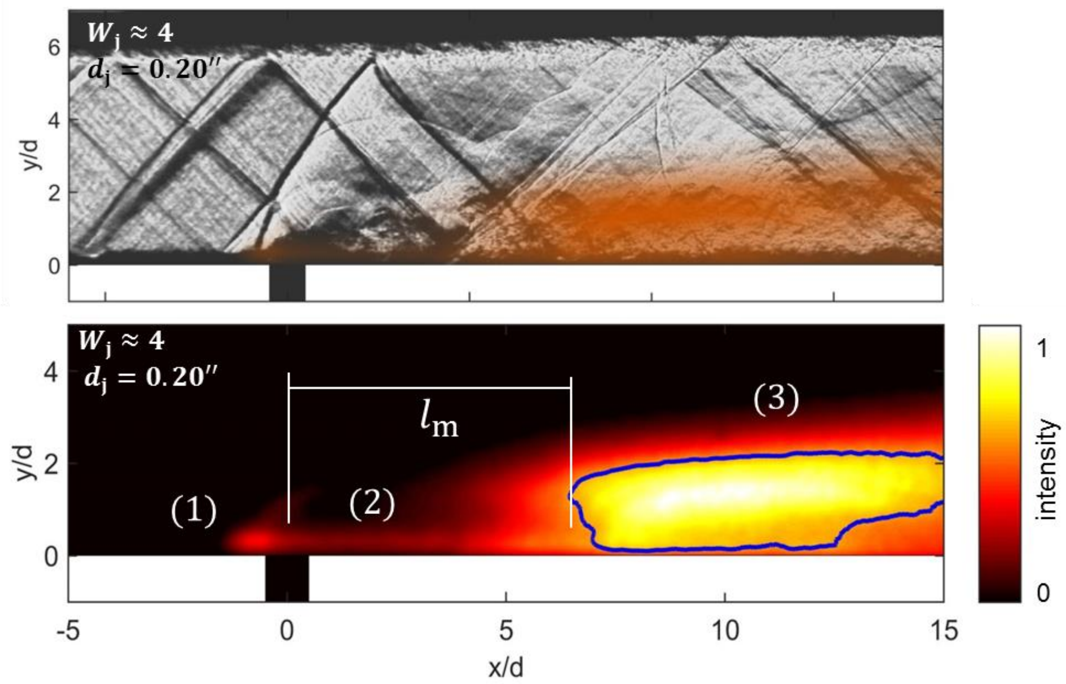

Figure 3. Transverse-jet injection into a supersonic N_2 crossflow stream with an inflow Mach number of $M_i = 1.5$. W_j denotes the jet-fluid (He) molar mass while $d_j = 0.20''$ is the jet diameter. Top: Single shadowgraph-schlieren digital image with a superimposed chemiluminescence image (from Cymbalist 2016, Fig. 2.15). Bottom: Frame-averaged chemiluminescence image from the same run (from Cymbalist 2016, Fig. 3.1). Color legend (bottom, right) registers intensity.

A separate investigation explored the possibility that the spatial delay is attributable to a mixing delay, which the chemical reaction must await before any significant reaction occurs. This was confirmed by an experimental investigation that varied the jet Reynolds number,

$$Re_j = \frac{\rho_j U_j d_j}{\mu_j}, \tag{2.1.1}$$

where ρ_j is the jet-fluid density, U_j is the jet velocity, d_j is the jet diameter, and μ_j is the jet (shear) viscosity, by varying the jet diameter as well as the jet-fluid density using a different mean molar mass for the jet fluid.

Figure 4 plots the delay length scaled by the (geometrical) jet diameter, ℓ_m/d_j, vs. a range in jet Reynolds number, in terms of $\log(Re_j)$. As can be seen, while the general trend suggests a Reynolds-number dependence and a fluid-mechanics cause for this delay, the plot does not indicate good collapse with respect to these parameters.

If the spatial delay is the result of turbulent mixing that occurs in the far field, however, the proper scaling length that also takes into account that the mean density in the jet becomes dominated by that of the entrained fluid is the jet-source diameter, i.e.,

$$d^* = \frac{2\dot{m}_j}{\sqrt{\pi \rho_\infty J_j}}, \tag{2.1.2}$$

where $\dot{m}_{\mathrm{j}}$ is the jet-fluid mass flux through the jet nozzle, ρ_∞ is the density of the far-field fluid that the jet entrains, and J_{j} is the jet momentum flux (thrust). These are integral quantities felt in the jet far field and parameterize entrainment and mixing far from the jet nozzle. This scaling is found to correlate jet flame lengths ranging from gas-phase reactions, to hydrocarbon combustion, to reacting jets in water. See Dimotakis (2000) and references therein.

Figure 5 plots the ratio of the delay length to d^*, vs. $\log(Re_{\mathrm{j}})$, indicating very good scaling in those terms and basically confirming that the spatial delay is attributable to turbulent mixing, as chemical reactions must await that process before proceeding.

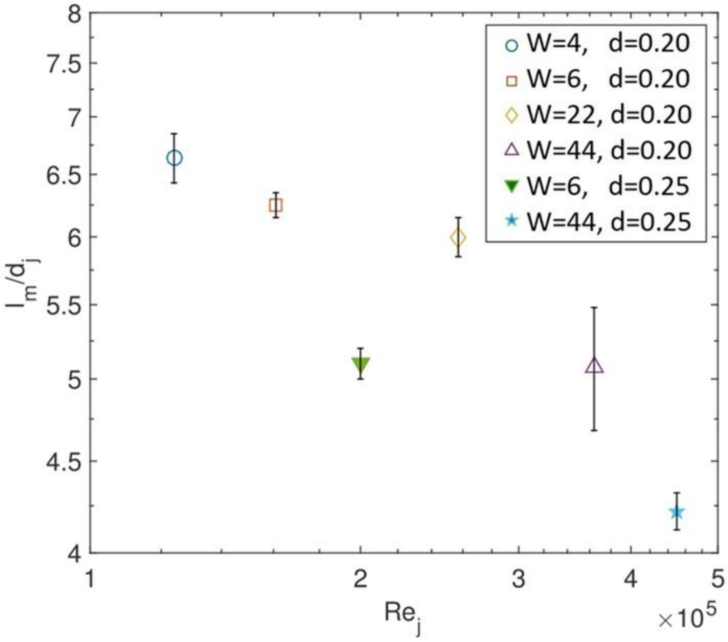

Figure 4. Mixing-delay length normalized in terms of the physical jet-orifice diameter, d_{j}, vs. the jet Reynolds number (Eq. 1). Bars reflect uncertainty based on the variation of ℓ_m.

Jet-inclination effects were studied by also investigating and comparing the behavior of normal jet injection ($\theta_{\mathrm{j}} = 90^{\mathrm{o}}$) with that of jets inclined at an angle of $\theta_{\mathrm{j}} = 30^{\mathrm{o}}$. Figure 6 compares the two cases for reacting jets, superimposing shadowgraph-schlieren data with chemiluminescence data and demonstrates the large difference in the cross-flow disturbance between normal injection and that from the inclined jet.

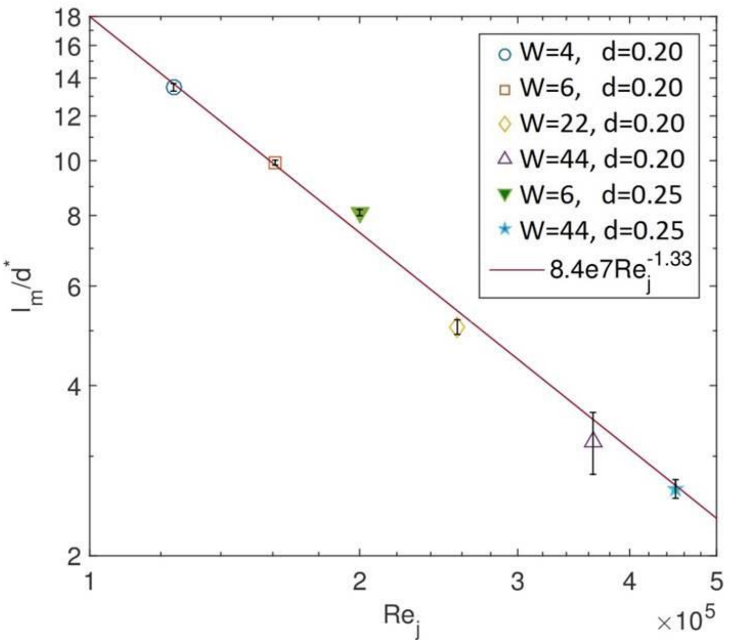

Figure 5. Variation of ℓ_m/d^* vs. jet Reynolds number (same data as in Figure 4).

This should help in scaling and design studies of scramjet combustor systems.

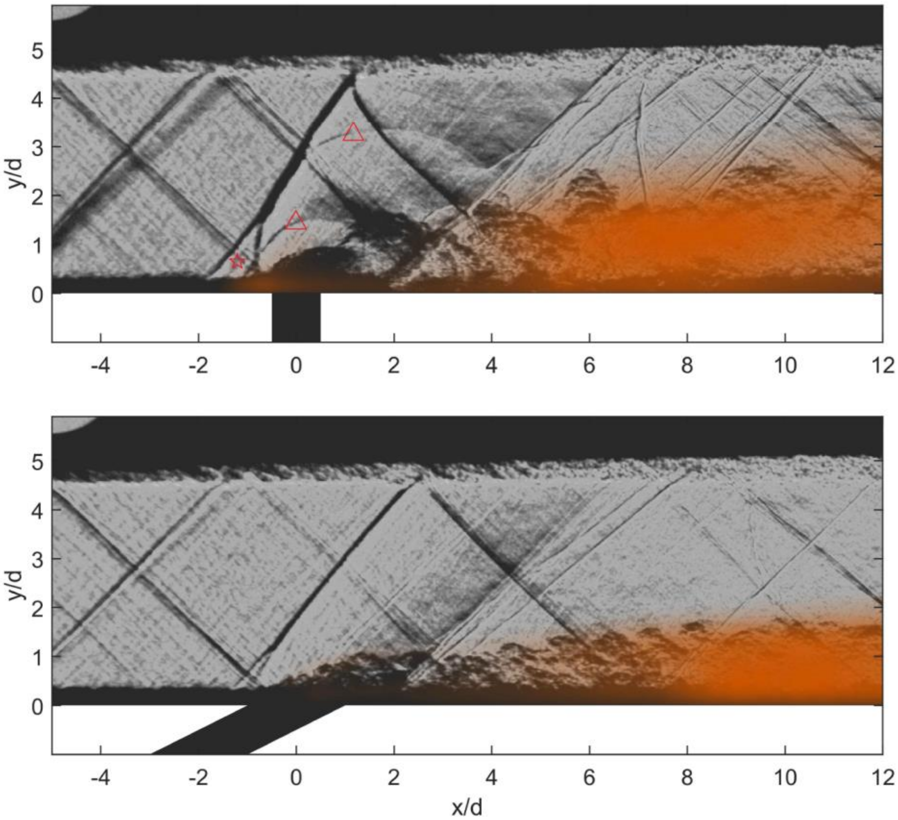

Figure 6. Superimposed shadowgraph-schlieren and chemiluminescence images of jet injection into a supersonic stream. Top: normal injection. Bottom: 30° inclined jet. The λ-shock structure ($*$ symbol) and acoustic waves (Δ symbols) are evident in the normal-jet case, but absent in the inclined-jet flow.

Figure 7 compares the corresponding (enhanced) chemiluminescence images for the two cases demonstrating the longer reaction-delay length for the inclined-jet case but also the lower penetration into the freestream, an important consideration for air-breathing scramjet propulsion. On the other hand, the deeper penetration of normal-jet injection is accompanied with considerable total-pressure losses, as can be inferred from the shock structure in Figure 6. Finally, we note that absent in the inclined-jet injection is a reaction zone upstream of the jet-injection station, indicating the difference in near-wall mixing and combustion between the two flows.

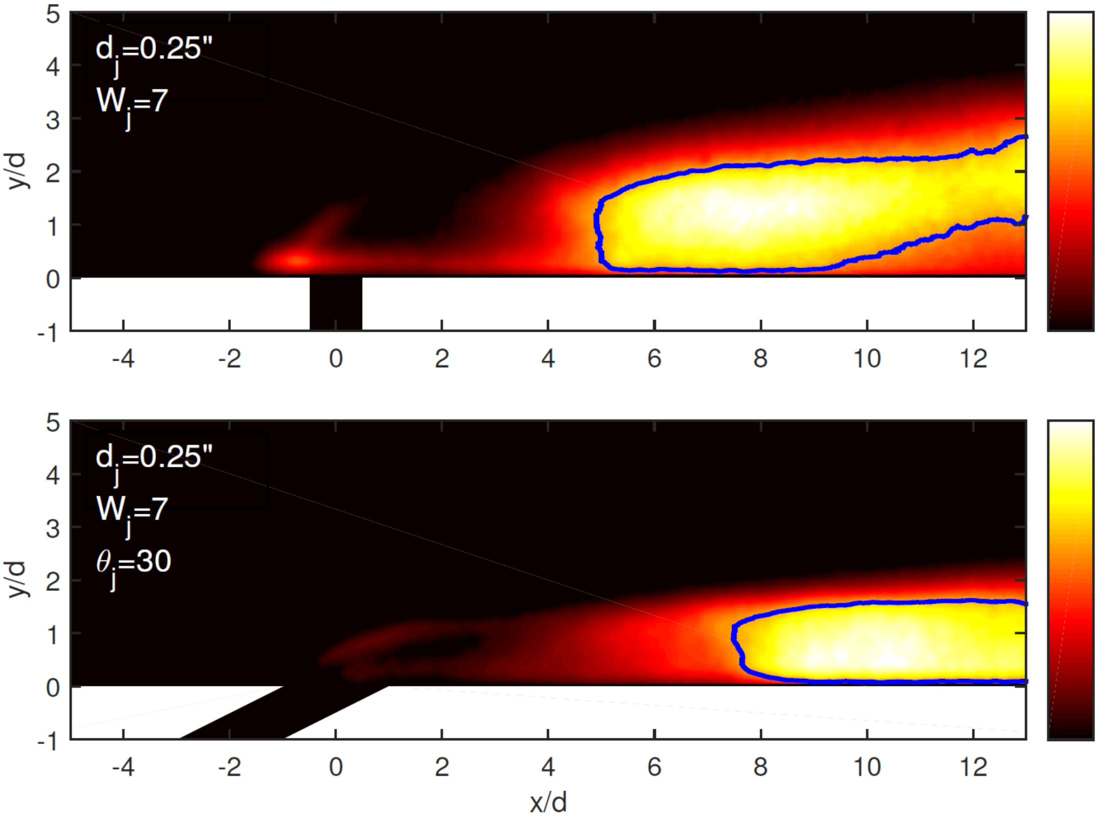

Figure 7. Chemiluminescence images from chemically reacting jets injected into a $M_{\mathrm{i}} = 1.5$ cross-flow. Top: normal injection ($\theta_{\mathrm{j}} = 90^{\mathrm{o}}$, same run as in Figure 3). Bottom: inclined injection at $\theta_{\mathrm{j}} = 30^{\mathrm{o}}$.

2.1.2 Experiments in small-scale mixing

Experiments in small-scale mixing continued under support of this grant, albeit at low priority in comparison to other focused efforts described in this report. Results from these experiments are shedding light into the small-scale scalar-mixing structure providing guidance to subgrid-scale (SGS) model development.

The experiments are conducted in water and rely on a facility (Figure 8) developed for the purpose to study the simplest turbulent flow, namely, grid-generated turbulence, with the capacity to generate a large range of Reynolds numbers based on the grid-mesh size, ℓ_{g}, i.e.,

$$500 \leq Re_M = \frac{U_g \ell_g}{\nu} \leq 56{,}000\,, \tag{2.1.3}$$

where U_g is the grid velocity, equivalent to the flow velocity in a water-tunnel frame, and ν is the kinematic viscosity. This Reynolds number range spans flows from below to above the mixing transition (Dimotakis 2000).

The experiments yield fully resolved 3D and 4D scalar-field data at the lower Reynolds numbers and a window to processes typically beyond experimental reach. Measurements rely on laser-induced fluorescence of a scalar tracer injected just downstream of the grid that then disperses and mixes in the ensuing grid-turbulence field. Custom-designed digital-imaging equipment and techniques developed starting with support by the NSF MRI Grant EIA-0079871 and the AFOSR DURIP award provided the instrumentation. Full-resolution measurements impose challenging data-acquisition and high-speed storage requirements derived from the sustained measurement rate of 2×10^8 measurements (pixels) per second. While such data rates are not uncommon today, what remains uncommon is the need to sustain them for many minutes to yield the data for the reconstruction of the required 3D and 4D fields. The experiments themselves were conducted (at low priority) under the AFOSR grant support documented in this report.

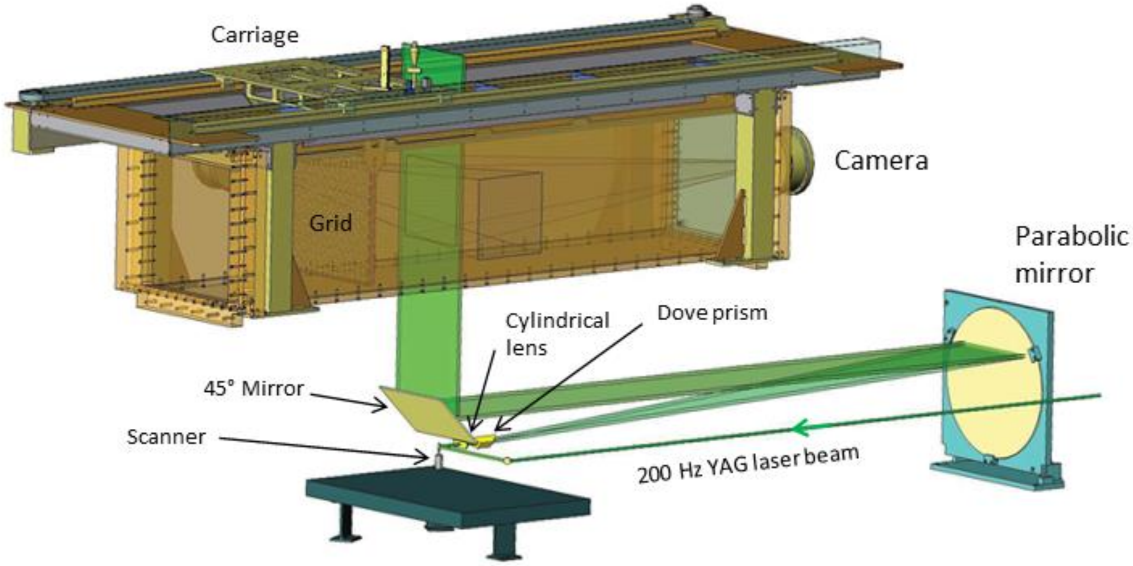

Figure 8. Grid-turbulence scalar-dispersion experimental facility.

The facility optics developed allow both streamwise and transverse cuts to be made by rotating a single Littrow prism, while retaining optical alignment. The parabolic mirror is an astronomical-quality reflector and produces a perfectly collimated beam obviating complicated image processing that was attempted in the early phases of this experiment.

Figure 9 below reproduces a streamwise cut of the scalar field and attests to the high signal-to-noise ratios and image quality attained. The field of view in this figure spans from, roughly, 16 to 24 grid-mesh lengths ($16 \leq x/M \leq 24$) downstream. The mesh Reynolds number is a little below the mixing transition. Evident in this image is the degree of unmixedness in this flow, with completely unmixed fluid crossing the full extent of the downstream scalar plume, as well as the very high local-instantaneous scalar-concentration values.

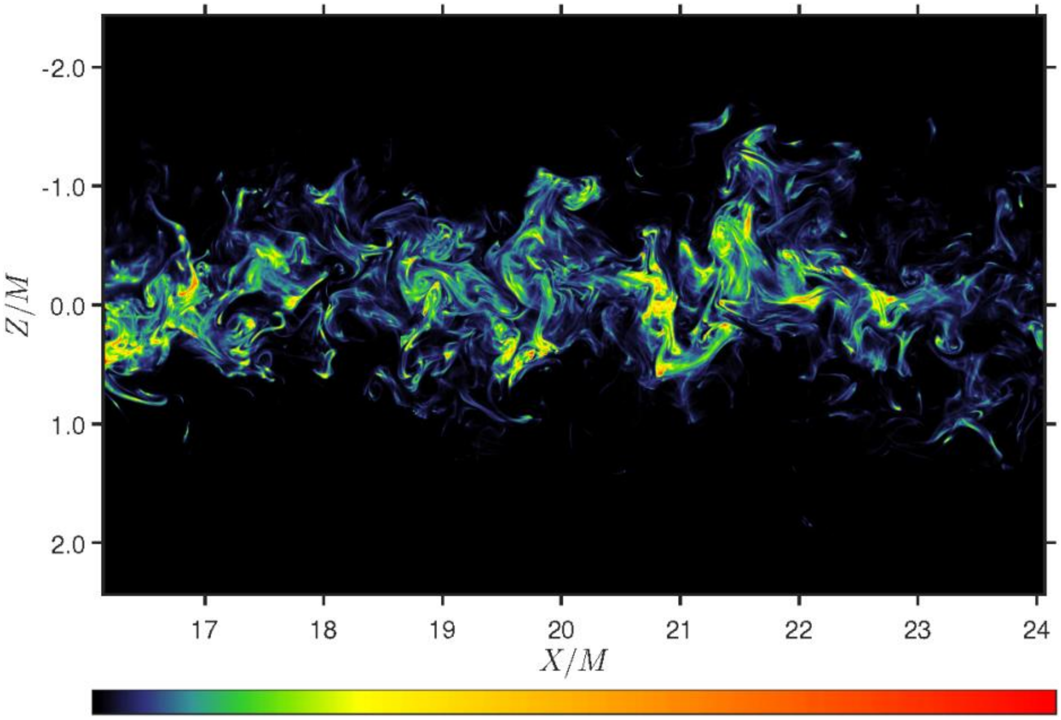

Figure 9. Scalar field vertical streamwise cut, $16 \leq x/M \leq 24$ downstream of the grid. Mesh Reynolds number, $Re_M \simeq 4200$. Color codes local scalar concentration (Dimotakis and Lang, unpublished data).

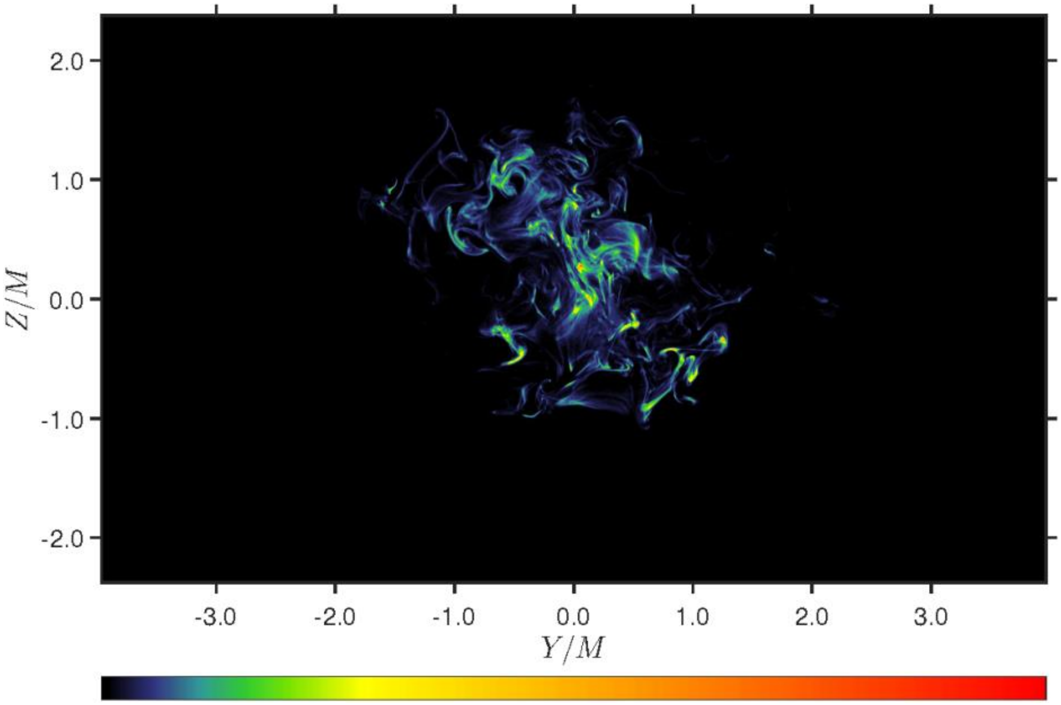

Figure 10. Scalar field vertical cross-stream cut, $x/M = 20$, downstream of the grid. Mesh Reynolds number, $Re_M \simeq 4200$. Color codes local scalar concentration (Dimotakis and Lang, unpublished data).

Cross-stream cuts were the most convenient to assemble to form the 3D images that are under investigation at this writing. An example of such a laser-sheet slice is reproduced in Figure 10, recorded at a distance $x/M \simeq 20$ downstream, mid-distance along the field-of-view that produced the data in Figure 9, at the same flow conditions that yielded the data in Figure 9.

Results indicate a qualitative transition in small-scale structure as the flow crosses the mixing transition, as can also generally be inferred from chemically reacting experiments sensitive to small-scale mixing.

This research is continuing as an unsupported effort at this writing, albeit slowly, and we hope to be able to document the important results in the near future.

2.2 New instrumentation, diagnostics, and experimental techniques

As part of the diagnostics-development effort, successive pairs of schlieren-shadowgraph images, spaced by a short interframe time interval ($\Delta t_{\mathrm{IF}} = 5 - 6\mu s$) apart, were correlated by extending previously employed methods to infer the velocity fields. Such correlations track the convection of index-of-refraction (IoR) interfaces in the flow, which can be discerned in Figure 3, top, and in Figure 6.

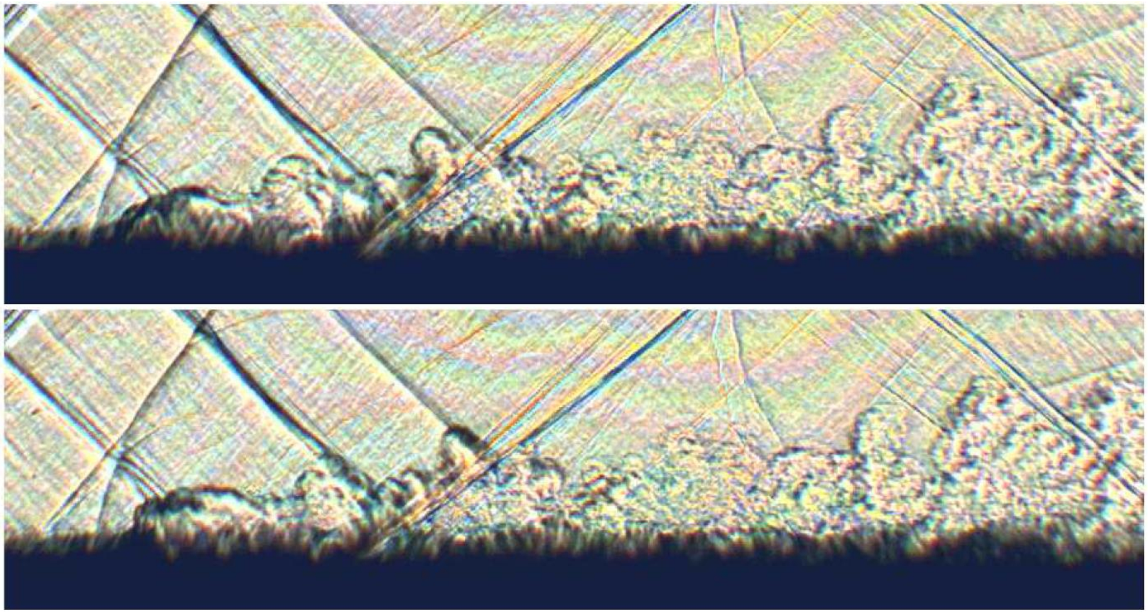

Figure 11. A-B image pair recorded spaced by an interfame time interval of $\Delta t_{IF} = 6\mu s$. Large-scale structures associated with the injected-jet flow convect (are approximately displaced in the streamwise direction) with little change in shape during such intervals.

Such correlation techniques have been proposed in the past (e.g., Townsend 1936) and employed in estimating convection velocities of flow structures in various flows, including supersonic flow (e.g., Papamoschou 1989), as well as in flow estimation for jets-in-crossflow (Gruber et al. 1997, Ben-Yakar et al., 2006). These methods relied on manual/subjective identification of flow structures used to track convection velocities. We decided to develop an objective velocity-estimation method instead, as described below.

Part of the challenge is that not all features in such images convect similarly, such as Mach waves that are (almost) stationary, boundary-layer structures that move with a fraction of the freestream velocity, etc. The technique developed more-closely derives from that of Jonassen et al. (2006), adapted for the special flows of interest here and the combination of flow structures that should and should not be taken into account.

A typical A-B image pair is shown in Figure 11, spaced by an interframe time of $\Delta t_{\mathrm{IF}} = 6\mu s$. Large-scale flow structures remain well-correlated across such short time intervals, while quasi-stationary structures registered as (almost) fixed in space and can be relatively easily removed from being considered for processing.

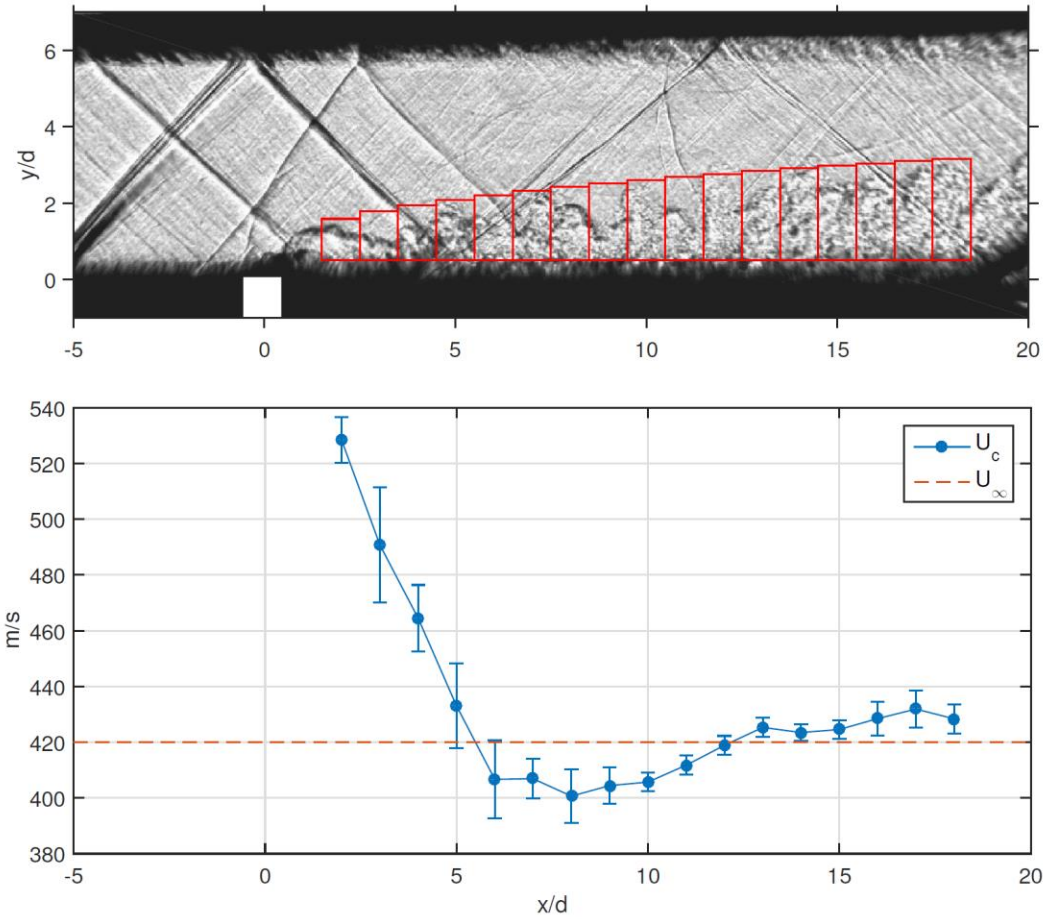

Figure 12. Binning structure (top) used to produce average convective velocity estimates (bottom).

The region downstream of the jet is binned into rectangular regions over which the schlieren-image correlation velocimetry (SICV) results are averaged to produce the convective-velocity estimates. The bins and typical results are shown in Figure 12. The freestream velocity can be reliably estimated from Mach-wave angles and is also indicated in the bottom panel of the figure.

An important conclusion is that velocities downstream of the supersonic-jet body quickly approach that of the freestream so turbulent mixing that ensues between the freestream and jet fluids takes place in an essentially incompressible (subsonic) flow environment. Further details and discussion can be found in Cymbalist (2016) and Cymbalist et al. (2017, in preparation).

Both shadowgraph-schlieren and convection-velocity experimental data were utilized in a novel way that relied on forward-modeling of beam propagation through the optical system (Figure 2) based on ray-tracing in the geometrical-optics approximation, as well the estimated convective velocity fields, as illustrated in the bottom panel of Figure 12.

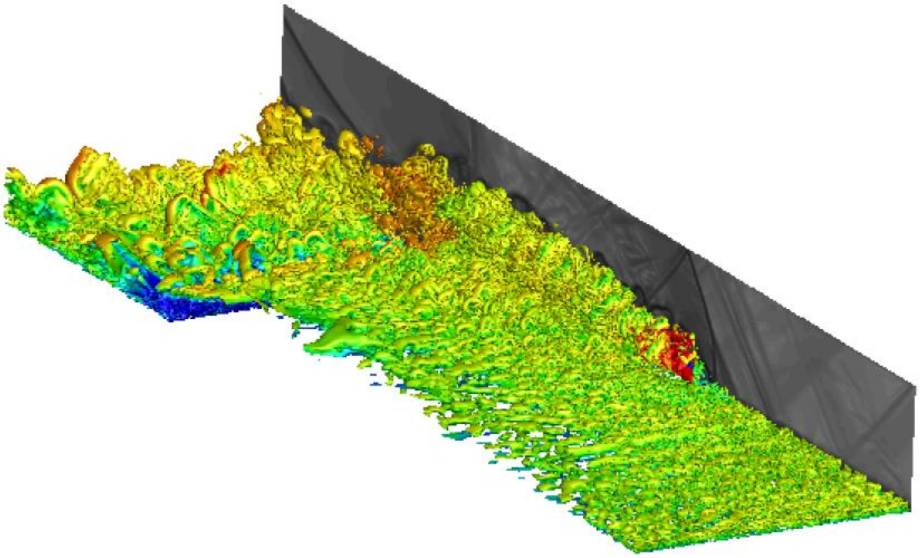

Figure 13. Half-volume results of the jet-injection LES modeling. Graphic plots isosurfaces of the Q-criterion colored by streamwise velocity.

The supersonic jet-injection flow was simulated using the US3D U. Minnesota code to produce instantaneous 3D flow fields, as depicted in Figure 13 that shows half-volume results of jet-injection LES modeling plotting isosurfaces of the Q-criterion colored by streamwise velocity.

The jet-injection region has the highest velocity (red) and crossflow is into the page. The center mid-span on the right plots contours of $|\nabla\rho|$ showing shock structures and eddy interfaces in this region.

Geometrical-optics forward modeling was then used to propagate the optical beam through all elements of the beam- and image-forming system, and though the instantaneous index-of-refraction (IoR) field in the turbulence to compute simulated shadowgraph-schlieren images. Typical results by way of illustration are shown in Figure 14.

In practice, an image is almost never a pure-shadowgraph or pure-schlieren image and the simulations also modeled how the knife-edge was set to match the optical choices made.

An important application of this technique was processing pairs of images computed based on the LES fields, as above, spaced by the same interframe time interval, and subjecting them to the same image-correlation velocimetry technique described above. This produced estimates of experimentally measured vs. computed velocity fields independently of each other.

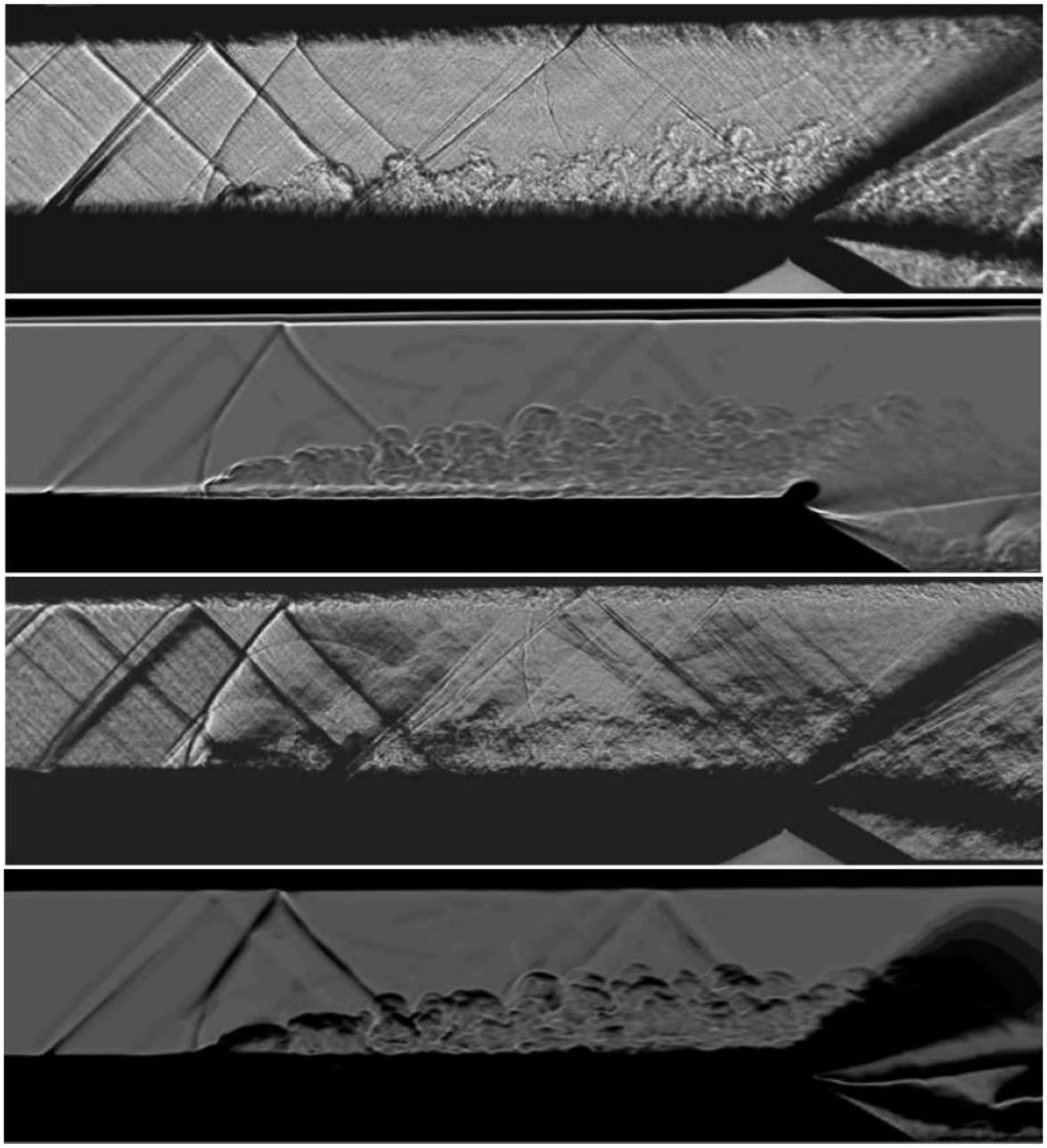

Figure 14. Experimental and computational schlieren and shadowgraph images. Top and upper middle: Experimental and computational shadowgraphs. Lower-middle and bottom: Experimental and computational schlieren.

Typical results are depicted in Figure 15 that allows a comparison of the two estimates. As can be seen, except for the region just downstream of the jet nozzle where the lower computational resolution did not allow the same degree of detail to be discerned, the results are in good agreement. Also in fairly good agreement is the jet-penetration extent. LES-SGS modeling options were not explored to investigate the relative merits of various SGS model options. Further details are documented in Luthman et al. (2017, in preparation).

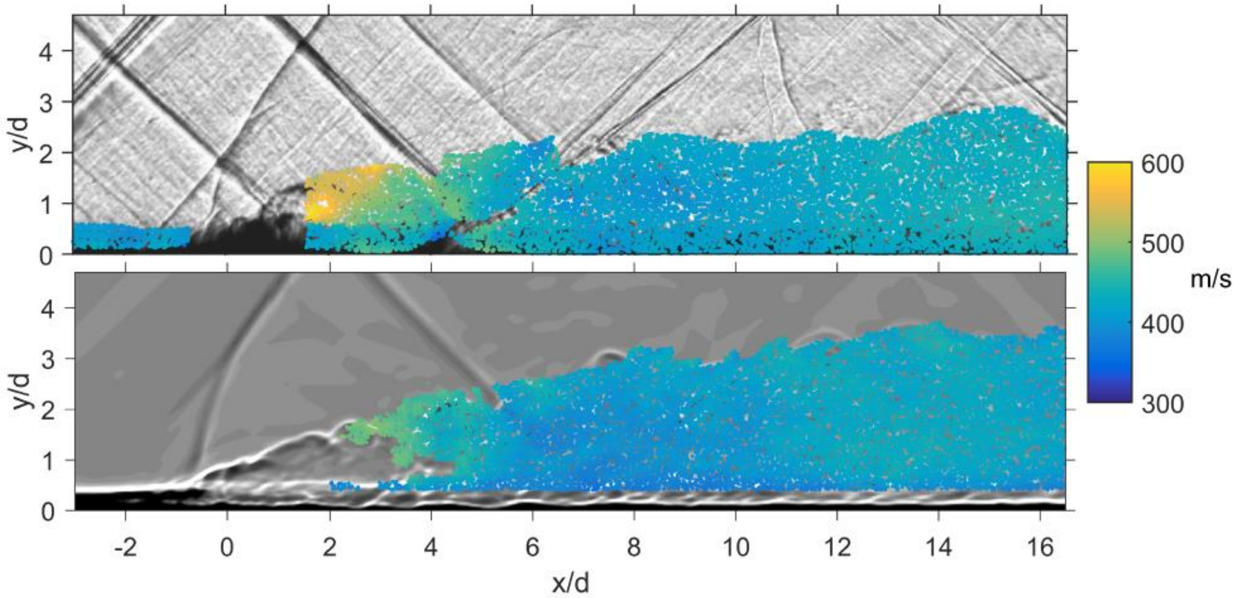

Figure 15. Streamwise velocity of convected refractive-index interfaces overlaid on an instantaneous shadowgraph under the same flow conditions. Top: experiment. Bottom:computation.

2.3 Large-scale direct numerical and large-eddy simulations

Part of the goal of the present research effort was not only to probe the behavior of flows with attributes relevant to high-speed air-breathing propulsion applications, but also to investigate generic fundamental behavior of flows that entail variations in density that cannot be ignored, as well as suitable subgrid-scale (SGS) models for use in large-eddy simulation (LES) modeling of such flows. To this end, direct numerical simulation (DNS) modeling, relying on spectral methods that are not subject to dispersion errors and which, in combination do not exhibit unphysical scalar excursions, was also part of the effort

2.3.1 Non-reacting variable-density compressible and incompressible flows

Direct numerical simulations (DNSs) that investigate fundamental characteristics of baroclinic vorticity generation that occurs in turbulent flows subject to externally imposed acceleration fields are in progress. In the context of the AFOSR research focus, such dynamics will be encountered when fluid parcels with density variations traverse an expansion zone in supersonic flow, as seen in the schlieren image in Figure 1 (Section 2.1.1), for example, or are accelerated through a contraction in subsonic flow. Very large (Lagrangian) accelerations can be imposed on the flow that are, of course, indistinguishable from any other acceleration field as far as the flow dynamics are concerned.

In variable-density flow, interactions between density and pressure gradients contribute to the generation of baroclinic torques as well as stabilization (stratification) or destabilization (Rayleigh-Taylor instability) effects that have no counterparts in uniform-density flows. Subgrid-scale (SGS) modeling was developed (Chung and Matheou 2014) but possible turbulence amplification by unstable configurations remains a research topic.

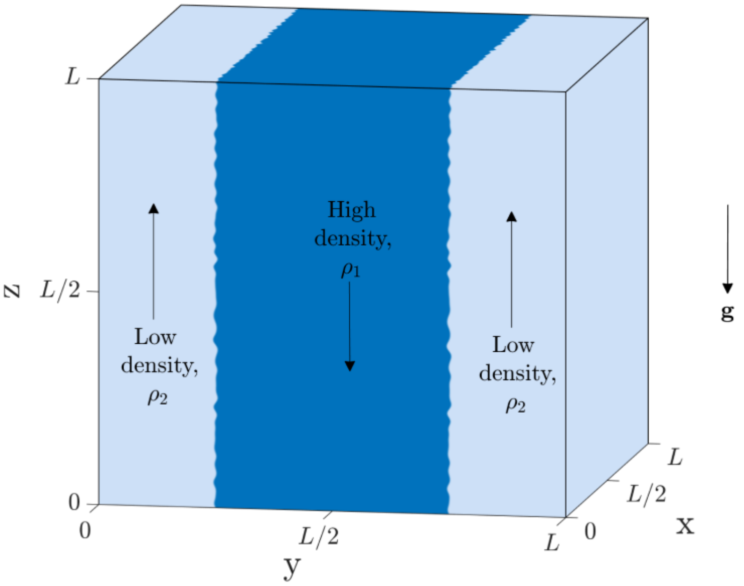

Figure 16. Initial density field and triply-periodic flow domain for the variable-density flow simulations.

The initial setup of the simulations performed is shown in Figure 16. The evolution of two fluid columns with different densities is simulated in a periodic domain. The initially quiescent fluids move under the force of an external acceleration field, which is perpendicular to the density gradient. This misalignment of the vertical hydrostatic pressure gradient and horizontal density gradient induces large-scale baroclinic torques in the turbulent shear-layers that ensue (Figure 17). Small-scale baroclinic torques are also generated in the turbulent zones as a consequence that would need to be accounted for in a LES.

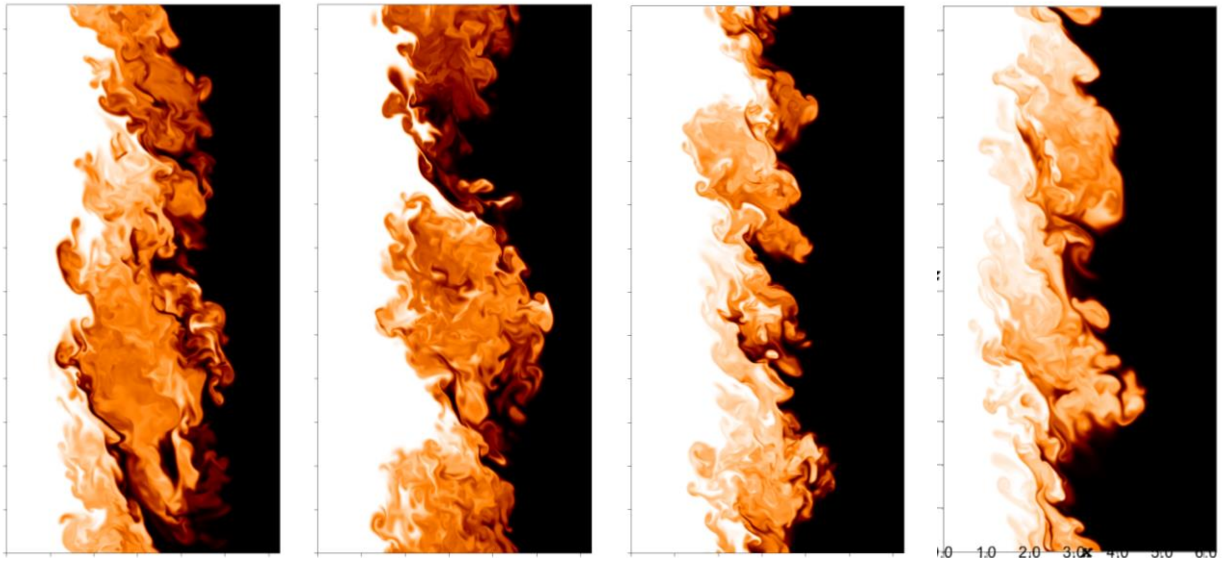

Figure 17. Density field snapshots on a vertical (x, z)-plane for density ratios (from left to right) of $R = \rho_1/\rho_2 = 1.4$, 2, 5, and 10, at time $t/\tau \simeq 0.3$. Black marks high-density fluid. Only half of the computational domain is shown. Color legends in each panel adjusted to span the entire density range.

Also important in the dynamics are instances when density and pressure gradients are (nearly) aligned and parallel, or (nearly) opposite. In such circumstances, the interaction of the two gradients leads to locally enhanced mixing, or flow stabilization, respectively.

Both baroclinic-torque generation and stabilization or destabilization of local fluid turbulence have no counterparts in uniform-density flows and must be accounted for in reliable LES modeling.

The evolution of two fluid columns with different densities is simulated in a periodic domain, allowing a full investigation of baroclinic effects. The flow is initialized in a quiescent state, with free streams developing relative motion in an external acceleration field in the vertical direction. Large-scale shear develops with a turbulent mixing zone between them (Figure 17). Large-scale misalignments of vertical pressure gradients and horizontal density gradients induce baroclinic torques.

Simulations at several density ratios have been carried out for $1.005 \leq R = \rho_1/\rho_2 \leq 10$, with numerical grid resolutions up to 1024^3. A density ratio of 10 poses considerable numerical-stability challenges and represents a significant accomplishment. The DNS relies on a pseudo-spectral numerical method that guarantees discrete mass conservation, regardless of iteration errors, e.g., Chung & Pullin 2010). The numerical calculation imposes a mean momentum that is constant in time, ensuring that no external forces other than gravity drive the flow. This is done by adding in a uniform pressure gradient, $\Gamma_i = - < \rho > g\delta_{i3}$, to the momentum equation, where $< \rho >$ is the mean fluid density in the domain. The momentum equation then becomes,

$$\mathrm{D}_t u_i = -\frac{1}{\rho}(\partial_i p + \Gamma_i) - g\delta_{i3} + \partial_j \tau_{ij} \,. \tag{2.3.1}$$

The term τ_{ij} in this equation is the viscous stress tensor, and $\mathrm{D}_t = \mathrm{D}/\mathrm{D}t = \partial/\partial t + (u \cdot \nabla)$ is the Lagrangian time-derivative operator.

The simulations assume a uniform Schmidt number of unity, i.e., $Sc = \mu/\rho\mathcal{D} = 1$, everywhere, where $\mathcal{D}$ is the species diffusivity. This produces comparable viscous and diffusion scales, but, because $\rho = \rho(\mathbf{x}, t)$, requires a diffusivity that is a function of space and time, with the dynamic viscosity, μ, assumed uniform.

The simulations verify the setup and show a flow evolving from an initially homogeneous and isotropic perturbation of the density interface (e.g., Cook & Dimotakis 2001, Cabot et al. 2005) to fully turbulent flow with spanwise-coherent structures, similar to uniform-density free-shear layers. Free-stream acceleration produces smallest (Kolmogorov) scales that decrease in size as time evolves, unlike free-shear layers with a constant freestream velocity difference. The viscosity is chosen for each DNS along with its grid resolution so the flow remains well resolved, with the maximum resolved (de-aliased) wavenumber and Kolmogorov scale, λ_K, such that $k_\mathrm{max}\lambda_\mathrm{K} > 1.5$, throughout the flow domain and during its evolution.

Figure 18 shows the evolution of the shear-/mixing-layer width, which exhibits a laminar (diffusive) evolution up to a normalized time $t/\tau \approx 0.2$, with $\tau \equiv 2\pi(l/\mathcal{A}g)^{1/2}$, where $l = L/2$

and L the spatial extent of the periodic domain, g the imposed acceleration magnitude, and $\mathcal{A} = (R-1)/(R+1)$ the Atwood number. Following transition to turbulence, the mixing-layer width δ, defined as the width within the mixture-fraction range of $0.01 < Y < 0.99$, where $(\rho_2 < \rho_1)$

$$Y(\mathbf{x}, t) = \frac{\dfrac{1}{\rho_2} - \dfrac{1}{\rho(\mathbf{x}, t)}}{\dfrac{1}{\rho_2} - \dfrac{1}{\rho_1}} \tag{2.3.2}$$

is the mass-fraction of high-density fluid in the mixture, and Reynolds number increase with time significantly faster following transition from the laminar-flow regime (Figure 18).

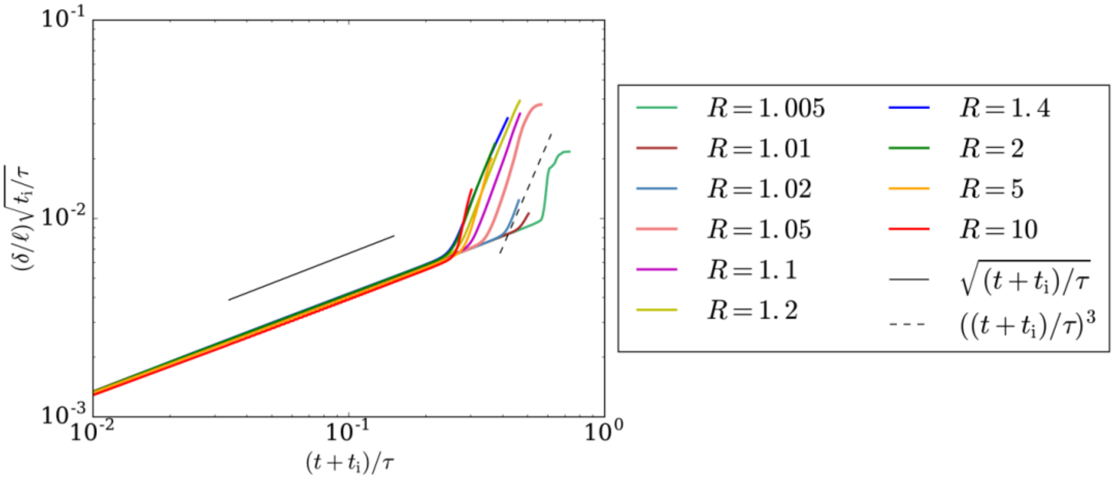

Figure 18. Non-dimensionalized shear-layer width, δ/l, scaled by the initial non-dimensional time. Colored lines are from simulations and black lines provide slope (growth-rate) references.

The simulations indicate an initial diffusive regime with a shear-layer width growth rate of $\delta(t) \propto t^{1/2}$, followed by a relatively sharp transition to a turbulent regime, in which shear-layer width increases as the cube of time, i.e., $\delta(t) \propto t^3$. Flow slices in Figure 17 correspond to this turbulent-flow regime.

Many turbulent flows grow linearly in space or time. Rayleigh-Taylor (RT) flows grow quadratically in time, i.e., $\delta_{\mathrm{RT}}(t) \propto t^2$ (e.g., Cook & Dimotakis 2001 and references therein). This flow exhibits a new turbulence regime that is the fastest-growing mixing region documented to date to our knowledge. Similarity and dimensional analysis arguments support the unique growth of the turbulent region in this flow environment.

Analytical results verified some of the bulk flow statistics, such as the time-dependent velocity difference across the growing shear layers free stream velocity (Figure 19, left), the mean density of the flow computed using the theoretical estimates of large-scale structure convection velocity (Dimotakis 1986), whose comparison with the DNS results is plotted in Figure 19, right), and the mixing-width evolution (Figure 18).

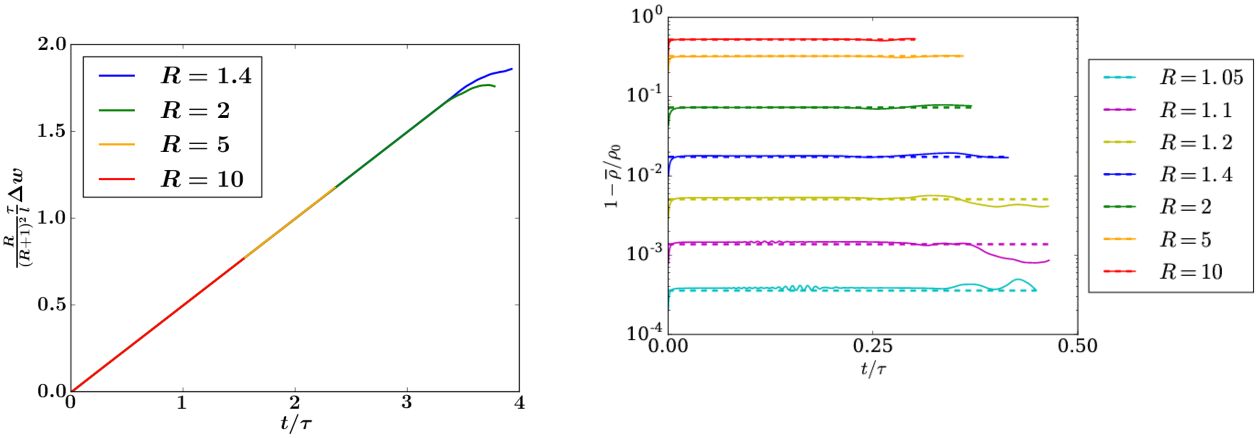

Figure 19. Time evolution of normalized free stream vertical velocity (left) and mean density within the mixing region (right). Solid lines denote numerical results and dashed lines denote analytical expectation.

Shear-layer mixing behavior depends on the freestream density ratio. Asymmetric entrainment is characteristic of a spatially developing shear layer for uniform-density flows. However, these simulations are of temporally developing shear layers and support asymmetric entrainment as a result of differences in freestream densities (Dimotakis 1986).

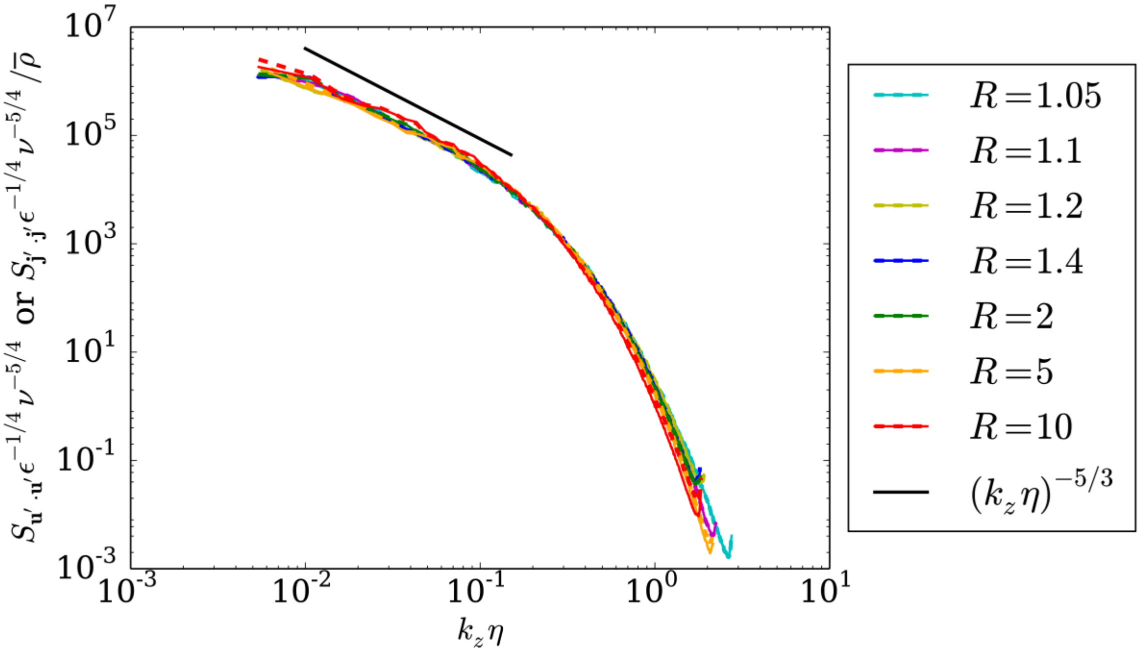

Figure 20. Specific kinetic energy spectra, $S_{\mathbf{u}\cdot\mathbf{u}}(k)$ (solid lines), and kinetic energy spectra, $S_{\mathbf{j}\cdot\mathbf{j}}(k)/\bar{\rho}$ (dashed lines), compiled at the same Reynolds number of $Re \simeq 8500$ in all cases, where $\mathbf{j} = \rho^{1/2}\mathbf{u}$ and $\mathbf{j}\cdot\mathbf{j} = \rho|\mathbf{u}\cdot\mathbf{u}| = \rho u^2$.

A challenge in variable-density flows has been how to resolve kinetic energy into its spectral components. For uniform-density flows, the Fourier transform of the autocorrelation of the scalar product of the velocity field, i.e., $S_{\mathbf{u}\cdot\mathbf{u}}(\mathbf{k}) = \mathcal{F}\{\langle\mathbf{u}(\mathbf{x}+\mathbf{r},t)\cdot\mathbf{u}(\mathbf{x},t)\rangle_{\mathbf{x},t}; \mathbf{r}\to\mathbf{k}\}$ in general, provides the wavenumber decomposition of $\mathbf{u}\cdot\mathbf{u} = u^2$, which is the *specific kinetic energy*. For uniform-density flow, this is simply multiplied by the uniform density to yield the kinetic energy.

The full kinetic energy in variable-density flow, however, is given by (1/2) of ρu^2. This challenge was addressed by considering the scaled velocity variable $\mathbf{j} = \rho^{1/2}\mathbf{u}$ (Kida and Orzag 1992), whose scalar product, $\mathbf{j} \cdot \mathbf{j} = \rho|\mathbf{u} \cdot \mathbf{u}| = \rho u^2$ then yields the desired quantity. This allows the spectral decomposition of the (full) kinetic energy of the variable density flow to be expressed as $S_{\mathbf{j}\cdot\mathbf{j}}(\mathbf{k}) = \mathcal{F}\{\langle \mathbf{j}(\mathbf{x}+\mathbf{r},t) \cdot \mathbf{j}(\mathbf{x},t)\rangle_{\mathbf{x},t}; \mathbf{r} \to \mathbf{k}\}$. This was then scaled by the mean density of the fluid, $\bar{\rho}$, i.e., $S_{\mathbf{j}\cdot\mathbf{j}}(k)/\bar{\rho}$, so it can be directly compared with the conventional (specific) kinetic energy spectrum. This comparison is plotted in Figure 20 and attests to the success of this velocity surrogate variable in bringing variable-density statistics in direct comparison with uniform-density-flow statistics.

These and other results have been presented and documented in the paper by Gat et al. (2016). A more-detailed paper with additional results and discussion is presently in preparation (Gat et al. 2017).

This part of the effort has been co-sponsored by the DOE Research Grant Award DE-NA0002382 and continues at this writing under its sponsorship.

2.3.2 Modeling and simulation of chemically reacting flows and combustion

Cymbalist and Dimotakis (2015) and Cymbalist (2016) proposed an approach to model high-speed combustion flows, including the effects of ignition delay and combustion in distributed-reaction zone (DRZ) regimes. Their evolution-variable manifold (EVM) approach explicitly captures and represents ignition delay and subsequent heat release as separate phases of combustion. Subgrid-scale combustion is represented by well-stirred reactors in unresolved computational cells that are given an initial condition and are integrated in time until they reach equilibrium. The time domain is then converted to a (Lagrangian) evolution variable, τ, that tracks the variation of the gas reactant state from an initial condition at $\tau = 0$ as it evolves to equilibrium at $\tau = 1$.[1] In the flow simulation, τ is computed as a field variable and its value represents the Lagrangian evolution of a reacting fluid element as it is transported, mixes, and reacts through the computational domain. The EVM approach pre-computes and tabulates the gas state as a low-order manifold in terms of the thermochemical state and reaction progress in terms of energy, density, mixture fraction, and the evolution variable.

A well-stirred reactor (WSR) model is expected to represent the small-scale structure of DRZ combustion and is used to generate the manifold based on either direct experimental data in the case of autoignition, or detailed kinetics models, to the extent these are known. With this approach, the complete thermochemical state of the gas is accessible to the flow field computation, making it possible to develop a numerical method that properly conserves energy in both compressible and incompressible flow, and is consistent with the evolving thermochemical state. Because the low-dimensional manifold that describes the combustion process is pre-computed, the EVM approach significantly reduces the simulation cost relative to

---

[1] The symbol τ in this section refers to the Lagrangian time of a fluid parcel that is transported and evolves, and is unrelated to the same symbol in the previous section that refers to the (fixed) time scale in the DNS computations.

full kinetics models and even relative to *in situ* tabulation based methods. Thus, the EVM approach has the potential to greatly reduce the cost and improve the reliability of large eddy simulation (LES) modeling of high-speed high Reynolds number turbulent-combustion flows.

Reliable simulation of high-speed turbulent combustion flows requires four modeling elements: compressible flow, near-wall turbulent motion, free or detached turbulent motion, and combustion progress including ignition-delay effects. In the research project, standard approaches were used for the first three elements, and focused on accurate and efficient modeling of turbulent combustion at conditions relevant to high-speed flight. To this end, an existing computational fluid-dynamics code was modified and extended (the University of Minnesota US3D code) for wall-modeled LES of compressible reacting flows to represent the detailed thermochemical state of a reacting fuel-air mixture, based on the reaction-evolution variable, a mixture-fraction variable, and the coupled thermodynamic state. The focus was on the development of a numerical method that is rigorously consistent with the thermochemical model so the numerical method correctly reflects the variations in the thermodynamic state. We applied the proposed numerical flux function to the supersonic reacting hydrogen injection experiments of Gamba and Mungal (2015) using the hydrogen-air chemical kinetics model of Burke et al. (2012). More recent simulations have involved the use of a data-driven tabulation of ethylene ignition delay time along with tabulated oxidation kinetics and wall-modeled large-eddy simulations of the University of Virginia dual-mode combustor configuration with ethylene fuel.

Developing the CFD methods so that the EVM approach could be implemented in a CFD code involved several steps and the use of a novel numerical flux function for high-order of accuracy simulations. For compressible flows, the thermodynamics and gas dynamics are tightly coupled, and this coupling must be done in a rigorously self-consistent fashion. With the EVM approach (and the standard flamelet-progress variable approach), the thermodynamic state is obtained from a table that is pre-computed at the relevant flow conditions. Thus, it was necessary to modify the CFD methodology to use the tabulated state and to compute all necessary thermodynamic variables from this state.

It was found that tabulating the chemical state as a function of the evolution variable τ, the mixture fraction Z, the gas density ρ, and the specific energy e, yields the most accurate and general approach. The rate of advance/production of τ is also tabulated. With this approach, all thermodynamic variables can be computed from the tabulated data, along with the transport properties (similar to Oevermann 2000). This approach is much more accurate and general than attempting to tabulate all required thermodynamic and transport property variables, as in Saghafian et al. (2015), for example.

Secondly, a new high-order (4th-order) convective flux formulation was developed that uses the tabulated information, yet produces a fully consistent numerical flux function. Here, the state of the gas at a cell face is constructed with high-order interpolants for species mass densities, velocity components, and pressure. Then, the face value of temperature is found from the equation of state of the local mixed gas constant and pressure, which is then used to construct the face value for the mixture energy. Next, the flux at the element face is computed. This is found to be much more accurate and robust than computing the energy in an approximate fashion. Details of this formulation are documented in Candler, Cymbalist, and Dimotakis (2017).

An additional consideration involved the treatment of the enthalpy flux attributable to mass diffusion. It was found that this term must be computed accurately based on the gradients of individual chemical species, rather than relying on approximations involving gradients of the evolution variable and mixture fraction. Without a correct evaluation of this term, unphysical bimodal temperature distributions across heat-release fronts may occur.

Extensive testing of the EVM-LES methodology was conducted. For example, the use of tabulated chemical species data was mimicked for simple one-step reactions to verify that the EVM code gives the same answer as the original code. These comparisons were instrumental in determining the correct approach for developing the numerical methods. As far as we know, such a method verification step has not been performed for previous implementations of the flamelet-progress variable approach, for example.

Many simulations with the LES-EVM approach have been performed. For example, Figure 21 plots the measured OH planar laser induced fluorescence (OH-PLIF) signal on the center plane of the Gamba and Mungal (2015) supersonic jet in crossflow experiments. Also plotted are several realizations of the computed OH-PLIF wall-modeled LES using the EVM-LES method/code developed as part of the AFOSR-funded research project described in this report. We have attempted to match the color map used to plot the experimental and computational data, however the experimental OH-PLIF was not calibrated, so quantitative comparisons are not possible.

Consistent with experiment, the EVM-LES predicts the presence of the thin flame front at the leading edge of the jet, along with more diffuse distributed combustion between the jet plume and the surface downstream of the injector. Detailed analysis of the Karlovitz number in this region confirms that the EVM approach is capable of predicting combustion in the distributed reaction (DRZ) regime.

Simulations of the University of Virginia combustor with ethylene fuel were also performed and are presently being analyzed and compared to the available experimental data. Initial results appear to be promising and we hope to document this part of the work in the future.

The EVM-LES method was demonstrated to be 4 times faster than a full 11-species chemical kinetics simulation for hydrogen-air combustion. For ethylene combustion, it is estimated that EVM-LES is about 12 times faster than using a skeletal mechanism such as in the work of Potturi and Edwards (2015). Incorporating a detailed full-kinetics ethylene-air model that would require transport all participating chemically reacting species would place such a simulation beyond present-day computational reach.

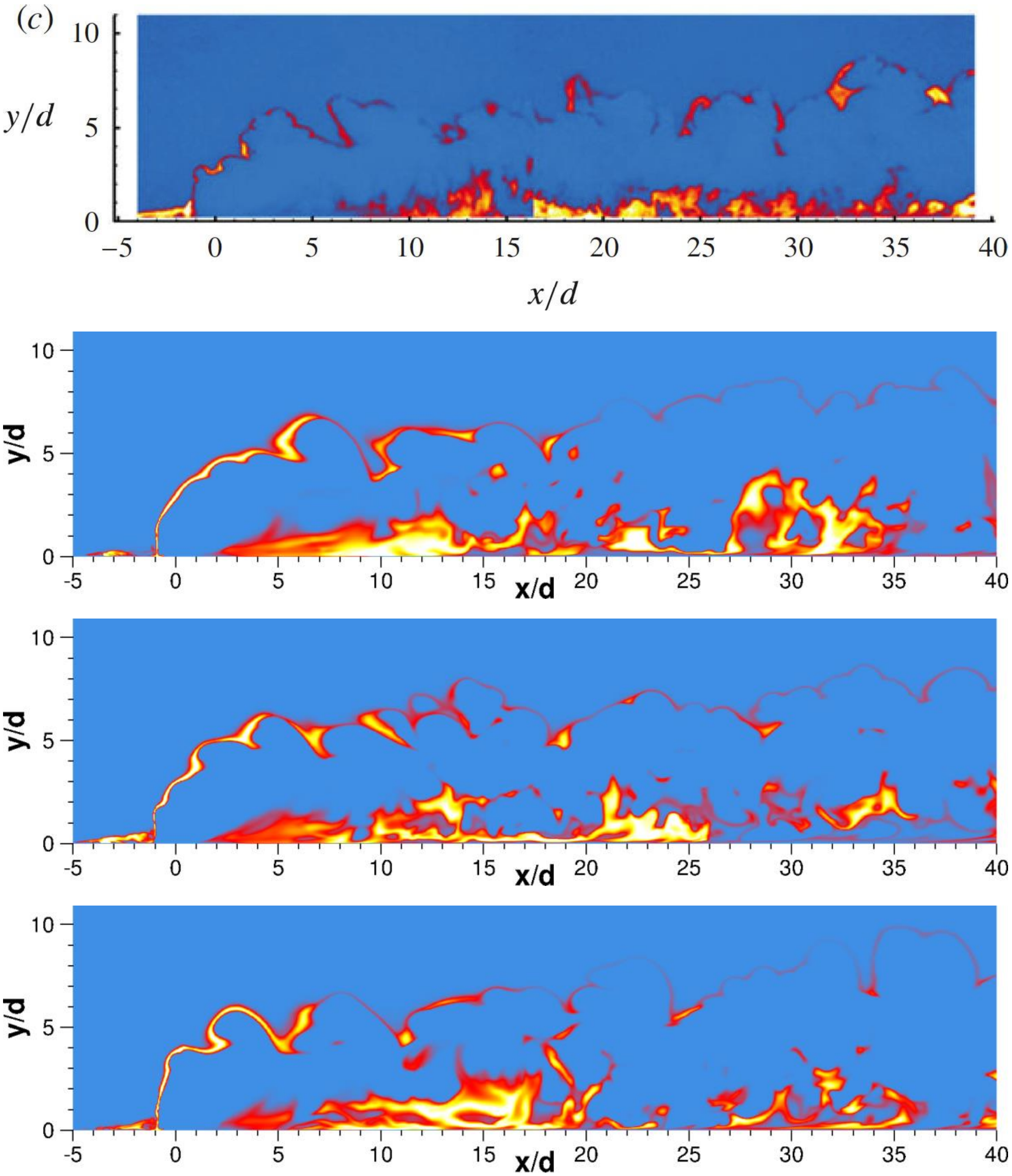

Figure 21. Centerline OH-PLIF images from the Gamba and Mungal (2015) experiment (top) and 3 images of the 107 million element wall-modeled LES-EVM separated by 50 μs in time.

Details of the integration of the EVM approach with the CFD code for wall-modeled LES are available in Candler, Cymbalist, and Dimotakis (2015, 2017), Cymbalist (2016), and Cymbalist, Candler, and Dimotakis (2016).

Extensive work was also conducted on the large-eddy simulation of two Caltech reacting hydrogen-fluorine mixing-layer experiments documented in the literature (Slessor et al. 1998 and Bonanos et al. 2008). Complete successful simulations of these flows have not yet been obtained for several reasons. The work is continuing, albeit slowly, and we anticipate that archival papers will be submitted on these simulations in the near term.

Issues encountered in the simulation of these flows led to important advancements in several areas; here the focus of the discussion is on the most important problem, spurious or unphysical numerical overshoots and undershoots in conserved scalars, as discussed in detail in Section 2.4, below. Additional difficulties were encountered with proper specification of the outflow boundary condition so that the exiting vertical flow does not interact with the flow. This problem was addressed by including a very large outflow domain to represent the experimental outflow expansion in the test-section duct and a portion of the dump tank, and the use of advanced boundary conditions from the literature. We also found that the breakdown of the mixing layer is extremely sensitive to inflow conditions and grid resolution in the vicinity of the splitter plate. This is not surprising since the initial instabilities that form near the inflow drive the rate of roll-up of the mixing layer. Unfortunately, this makes the simulations very difficult because small changes to inflow boundary-layer properties can produce substantially different results. We have used digital filtering approaches to provide physically meaningful inflow data for turbulent boundary layers. While this improved comparisons with experiment, we are still studying this problem to fully understand how to best impose conditions provided by the state of the inflow boundary layers.

2.4 Unphysical scalar excursions in finite-difference LES modeling

Unphysical scalar excursions were mentioned in the discussion above are responsible for significant challenges in the simulation of turbulent mixing, chemically reacting flows, and combustion. A discussion of the issues follows below. Further details are documented in the publications cited.

2.4.1 Excursions in passive-scalar transport

The LES equation for a resolved passive scalar field, $\bar{Z}(x,y,z,t)$, is given by (summation-convention implied),

$$\partial_t \bar{Z} + \partial_j \left(\bar{u}_j \bar{Z} \right) = \mathcal{D} \partial_{jj}^2 \bar{Z} - \partial_j \sigma_j \,, \tag{2.4.1}$$

where $\bar{\mathbf{u}}(x,y,z,t) = \hat{\mathbf{j}} \bar{u}_j(x,y,z,t)$ is the vector flow velocity, $\mathcal{D}$ is the scalar-species diffusivity (here assumed constant and uniform), ∂_{jj}^2 is the Laplacian, and $\boldsymbol{\sigma}(x,y,z,t) = \hat{\mathbf{j}} \sigma_j(x,y,z,t)$ is the SGS scalar flux.

Solutions to Eq. (2.4.1) must satisfy the maximum principle i.e., a $\bar{Z}$ field that is bounded in the flow domain by its initial and boundary values. In practice, numerical solutions to Eq. (2.4.1) obtained from difference methods incur dispersion errors that result in unphysical scalar excursions, in violation of the maximum principle.

Matheou & Dimotakis (2014, 2016) reported on the extent of such violations incurred with several numerical schemes for a LES modeling of a temporally evolving turbulent 3D shear layer at high Reynolds numbers. It was found that the fully conservative schemes of Morinishi *et al*. (1998), where the truncation error term is dispersive, generate maximum excursions whereas the flux-limited approach using the first-order upwind and the Lax-Wendroff method, because of their diffusive nature, suppressed excursions. However, diffusive schemes that rely on numerical dissipation, i.e., added artificial diffusion, can over-estimate mixing, presenting a serious challenge to reliable (predictive) numerical simulations.

Scalar excursions were studied in a triply periodic shear flow arranged in a vertically periodic stack of mixing layers (Figure 22). Three parameters were varied in the LES runs: the discretization of the convection terms, grid resolution, and the SGS model type, including model parameters. Two types of scalar boundedness error were studied: global and local (or internal) unphysical scalar excursions. Global excursions correspond to violations of the minimum and maximum principle with respect to the initial and boundary conditions. That is, any scalar value that is less or larger than the boundary values, e.g., mixture fraction values $\bar{Z} < 0$, or $\bar{Z} > 1$. Local excursions are defined as violations of the scalar boundedness property in the mixed fluid, i.e., $0 < \bar{Z} < 1$.

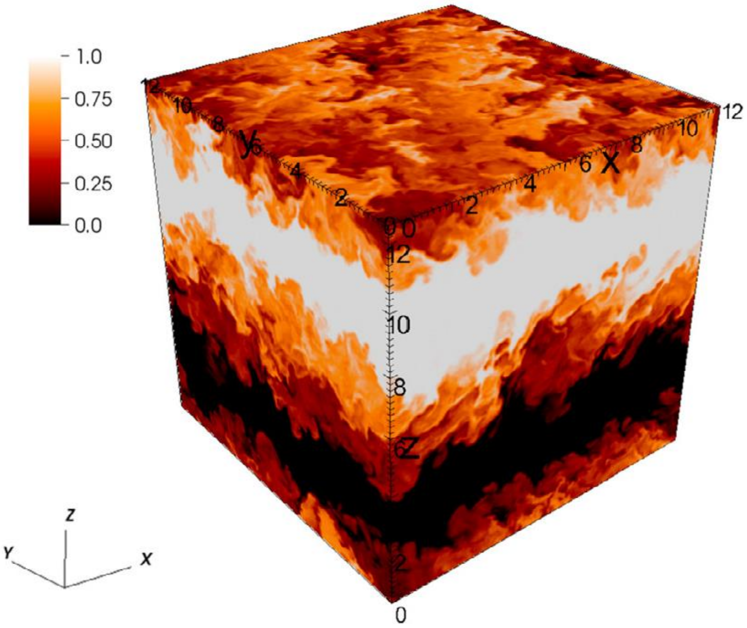

Figure 22. Evolution of the passive scalar field. Graphic computed for $t = 20\text{s}$. $\bar{Z} = 1$ (white) fluid moves from left to right with a freestream speed of $U = +1\ \text{m/s}$. $\bar{Z} = 0$ fluid (black) moves from right to left with $U = -1\ \text{m/s}$.

Global excursions are straightforward to diagnose and compile error metrics and their characteristics. They were analyzed by considering the minimum and maximum in the entire computational domain and the volume of fluid with scalar values exceeding an excursion threshold. For a family of non-dissipative fully conservative schemes (Morinishi *et al*. 1998), excursions decrease as the order of accuracy of the numerical approximation increases. A Quadratic Upstream Interpolation for Convective Kinematics (QUICK, Leonard 1979), which is a linear upwinding scheme, results in smaller excursions than non-dissipative schemes. A flux-limited monotone scheme is also assessed and, as expected, no scalar excursions are observed. Global unphysical scalar-excursion statistics are found to strongly depend on the SGS model and model parameters.

Two SGS models were assessed, the stretched-vortex model (SVM), documented in a series of papers by Pullin, Saffman and co-workers, and a constant-coefficient Smagorinsky (1963) model. The excursions are significantly reduced when the characteristic SGS scale is set to twice the grid spacing in runs with the stretched-vortex model, even though that requires a (considerably) greater computational effort. Maximum global unphysical excursions and volume fraction show opposite trends with respect to resolution. The maximum excursion increases as resolution increases, whereas the volume fraction decreases, as might be expected on the basis of statistics; the number of grid points and sample size increases with resolution. In contrast, the volume fraction of unphysical excursions decreases with resolution because the SGS models perform better at higher grid resolutions.

Local-excursion characteristics are defined with respect to the local non-diffusive limit. To define a local excursion, the scalar-transport equation is integrated in time from an initial state, *t*, for a short time interval Δ*t*, i.e.,

$$\int_t^{t+\Delta t} \partial_t \bar{Z}\,\mathrm{d}t + \int_t^{t+\Delta t} \partial_i (u_i \bar{Z})\,\mathrm{d}t = \mathcal{D} \int_t^{t+\Delta t} \partial_{ii}^2 \bar{Z}\,\mathrm{d}t. \tag{2.4.2}$$

The value of Z at $t + \Delta t$ depends on contributions to Z_t from convection and diffusion, i.e.,

$$\bar{Z}_{t+\Delta t} = Z_t - \int_t^{t+\Delta t} \partial_i (u_i \bar{Z})\,\mathrm{d}t + \mathcal{D} \int_t^{t+\Delta t} \partial_{ii}^2 \bar{Z}\,\mathrm{d}t. \tag{2.4.3}$$

In the limit of vanishing positive diffusivity, $\mathcal{D} \to 0^+$, the sign of the diffusive term determines the relation of $\bar{Z}_{t+\Delta t}$ with respect to the non-diffusive limit. Thus, the local constraint of the Eulerian $\bar{Z}$ is,

$$\bar{Z}_{t+\Delta t} > \operatorname{sign}\left(\int_t^{t+\Delta t} \partial_{ii}^2 \bar{Z} \mathrm{d}t\right)\left(\bar{Z}_t - \int_t^{t+\Delta t} \partial_i (u_i \bar{Z}) \mathrm{d}t\right) \equiv \bar{Z}_{\Delta t,\mathrm{nd}}\,, \tag{2.4.4}$$

where the right-hand side denotes the non-diffusive short-time estimate. This constraint is local in space and time and results in the requirement that only local mixing/diffusion of $\bar{Z}$ is allowed. That is, it requires that local $\bar{Z}$ values must be on the “convex side” of the non-diffusive limit.

To diagnose (2.4.4) in LES, the convection term must be computed sufficiently accurately for an interval Δ*t*, which requires performing an inviscid integration. A more-accurate inviscid integration for the scalar is performed on a finer grid. In the present runs, we utilize a refinement factor of 4, i.e., $\Delta x_{\mathrm{fine}} = \Delta x/4$, for diagnostic purposes.

At time t, velocity and scalar fields are interpolated on the fine grid using trilinear interpolation, which preserves total mass. The scalar equation on the fine grid is then integrated for time Δt using the current fine-grid-interpolated velocity field at each sub-step of the Runge–Kutta. This process results in the RHS of (2.4.4), i.e., $\bar{Z}_{\Delta \mathrm{t,nd}}$. Constraint (2.4.4) is then evaluated by comparing the co-located $\bar{Z}_{\Delta \mathrm{t,nd}}$ on the fine grid and $\bar{Z}$ on the original (coarse) LES grid. No averaging is performed from fine to coarse grids, because this would result in diffusion of the fine-grid $\bar{Z}$-field and invalidate the inviscid nature of the integration that is required.

Figure 23 shows the frequency distribution (i.e., the two-dimensional histogram) of the local excursion–scalar gradient pairs for 11 flow realizations in the $t = 10\text{–}20$ s interval, for a run with 256^3 grid points, fourth-order convection, and the stretched-vortex model. Unphysical excursions (y-axis) are relatively rare and about 97% of the occurrences are accounted for in the $y = 0$ bins in the histograms of Figure 23, corresponding to the dark band along the x-axis. The pairing/association of excursions to scalar gradient is done in two ways: using co-located pairs (Figure 23, left panel) and by pairing each excursion value with the maximum gradient magnitude in the surrounding 7×7×7 grid cells (Figure 23, right panel). This is to account for the offset of the maximum dispersion error with respect to the local gradient, which is usually 2–3 grid cells. The joint histograms in Figure 23 show that excursions and scalar gradient magnitude are not well correlated. Even when accounting for non-colocation, maximum excursions tend to occur at intermediate values of scalar-gradient magnitude. Moreover, for a given scalar excursion value, the gradient distribution is broad.

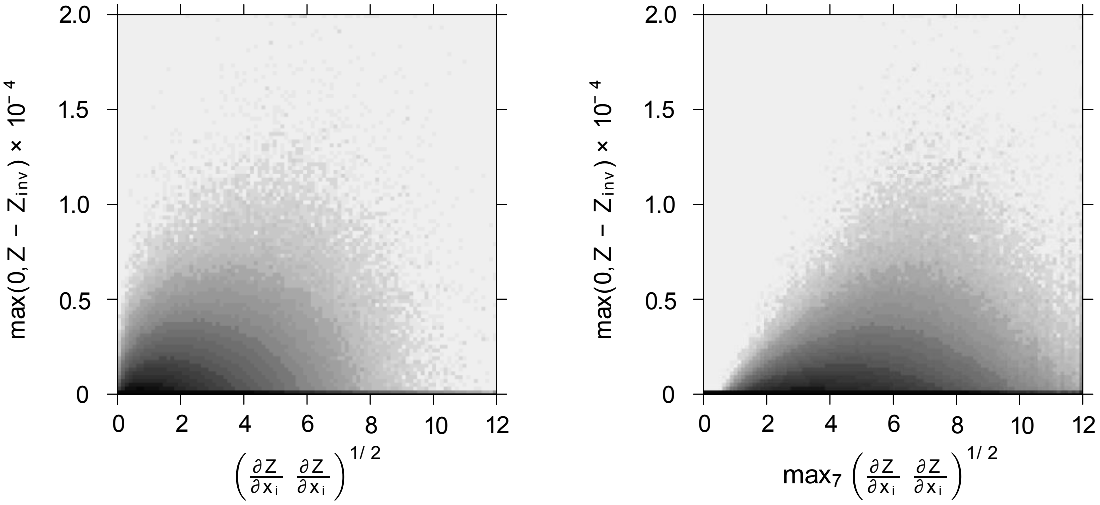

Figure 23. Two-dimensional frequency distributions of local excursion–scalar gradient pairs for 11 flow realizations in $t = 10\text{–}20$s for a run with 256^3 grid points, fourth order-convection and the stretched-vortex model. Darker shades correspond to higher frequency. Frequency values span a large range of scales and contours are logarithmically spaced, i.e., $\log(h + 1)$, where h is the frequency of occurrence of a given pair. Left panel shows co-located pairs. Right panel shows excursions paired with the maximum scalar gradient magnitude in surrounding 7×7×7 grid cells.

Figure 24 shows the frequency distribution of the local excursions and estimate of the scalar-dissipation rate. Unlike the local-excursion and scalar-gradient pairs in Figure 23, a significant fraction of local unphysical excursions can be seen to occur near grid points with low scalar dissipation values. There is a very small fraction of grid points with (unphysical) negative dissipation rates but for most of these points no unphysical excursions are observed (contour scales in Figure 23 and Figure 24 are with a logarithmic spacing). The right panel of Figure 24 shows pairs of scalar excursions with the minimum dissipation in the surrounding 7 × 7 × 7 grid cells (similar to the right panel of Figure 23). All grid cells with unphysical scalar excursions are at a distance less than 4 grid cells from locations with near-zero scalar-dissipation rate.

The analysis of scalar-excursion statistics shows that unphysical scalar excursions in LES result from dispersive oscillations of the convection-term discretization at times and locations where the subgrid-scale model provides insufficient dissipation to produce a sufficiently smooth scalar field. Further details are provided in Matheou & Dimotakis (2016). A conclusion of that work is that further improvements in SGS models can mitigate and may be required to address unphysical scalar excursions.

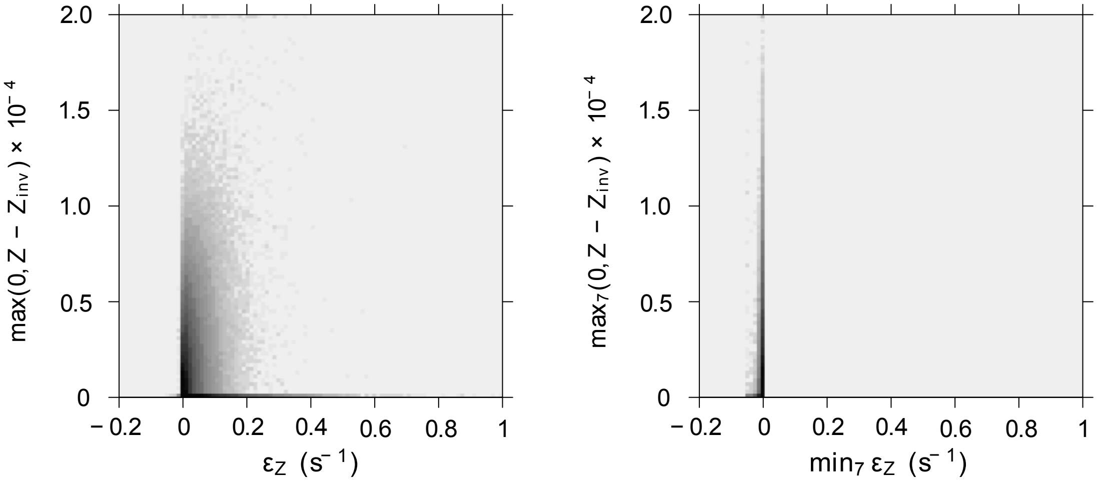

Figure 24. Two-dimensional distributions of local excursion and scalar-dissipation-rate pairs for 11 flow realizations in $t = 10–20\mathrm{s}$ for runs with 256^3 grid points, 4th-order convection and stretched-vortex model. Darker shades correspond to higher frequencies. Contour levels are the same as in Figure 23. Frequency values span a large range of scales and contours are logarithmically spaced, i.e., $\log(h + 1)$, where h is the frequency of occurrence of a given pair. Left panel shows co-located pairs. Right panel shows excursions paired with the minimum scalar-dissipation rate in the surrounding 7 × 7 × 7 grid cells.

The causes leading to insufficient SGS scalar dissipation are currently not well understood. Moreover, it is not clear if the problem originates from the momentum SGS modeling or only affects the scalar fields, implying a breakdown in assumptions that relate the turbulent momentum and scalar fields. Even though the scalar excursion volumetric error is small, its nature can lead to compounded errors in LES involving active scalars. Higher order non-dissipative finite-difference discretizations do not yield fast error reduction, while low-order discretizations produce excessively high errors, and general dissipative schemes must be regarded as a blunt tool, since they introduce artificial dissipation in locations where the SGS model may already provide the necessary dissipation.

2.4.2 Unphysical excursions in active-scalar transport

In an extension of this research to active scalars, it was noted that unphysical scalar excursions were responsible for the major bottleneck associated with the simulation of the Caltech HF experiments (Subbareddy et al. 2014; Ferrero et al. 2013; Kartha et al. 2014, 2015). This has relevance to many reacting-flow simulations where unphysical undershoots and overshoots may occur in species mass fractions or other scalars that must be rigorously bounded. This is a particular problem for compressible LES where interfaces between different gas types are usually poorly resolved by the grid. The high-order (fourth-order, or higher) methods required for LES often produce spurious values of scalars across these interfaces. During the research project, we worked to eliminate this type of numerical error; we have now developed and tested a new limiting approach that allows spatially fourth- and sixth-order accurate solutions to be obtained. Two papers are nearing completion on this work.

Physical bounds of conserved scalar values set by the initial and boundary values of a simulation are not violated. For instance, the numerical method must guarantee that the mass fractions of chemical species are individually in the range [0,1] and sum to unity. In a reacting gas, species mass fractions must also be bounded, but their limiting values are not set by the boundary conditions. This makes it much more difficult to control spurious mass-fraction values. Naïvely correcting deviations generally results in a scheme that does not conserve mass.

The use of spatially high-order methods in reacting flow calculations often results in local undershoots and overshoots in the species mass fractions, causing unphysical results. This results in mass-fraction or other scalar non-conservation. For reacting cases, these errors can cause temperature to exceed the adiabatic-flame temperature or violate other physical constraints.

We have developed a switched, low-dissipation numerical-flux methodology suitable for scalar conservation laws in compressible flow. For passive scalars, the approach uses a decoupled flux that combines several ideas from the literature and produces bounded results with acceptable levels of numerical diffusion. For the species fluxes (active scalars), we have developed an efficient novel low-dissipation method. A few heuristic choices, involving the low-dissipation switch and the jump detectors are made: these parameters can be tuned for specific applications.

Figure 25 presents a comparison for two sixth-order accurate flux methods for a one-dimensional test case involving large variations in the thermodynamic properties and the mass fractions. Note that the improved numerical flux function eliminates the spurious variations in the plotted species mass fraction that pervades and corrupts the solution for the original numerical flux.

Additional multi-dimensional test cases show that the proposed approach is also valid for more complex flows. To evaluate the performance of the new method for cases with variations in mass-fraction and thermodynamic properties, we perform test simulations reported in literature. These cases include a two-dimensional temporal mixing layer with multiple species and a shock/density-bubble interaction that shows very good comparison with literature results. Thus, we have found that the method produces results with well-behaved variations in the species-densities and temperature, and the results improve with increasing grid refinement.

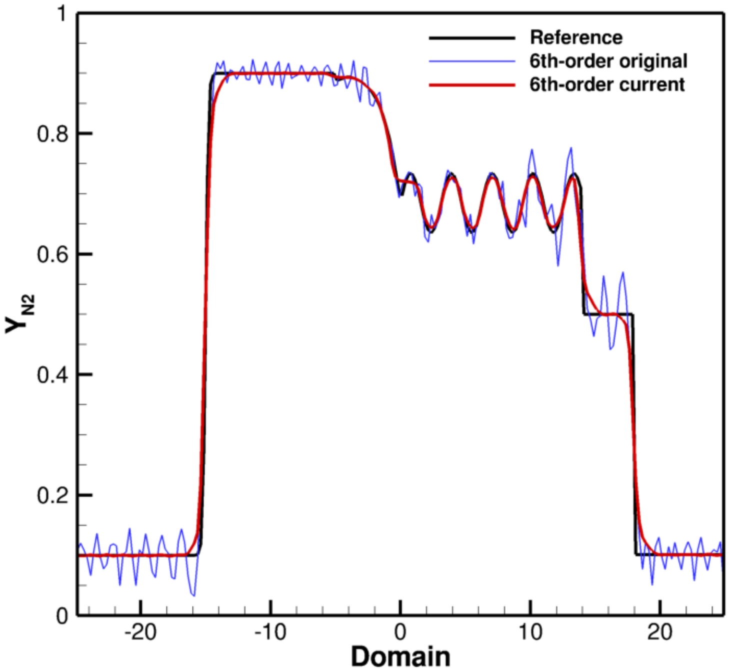

Figure 25. Comparison between the original and improved 6th-order accurate fluxes for a one-dimensional flow with large density, temperature and mass fraction variations.

To further evaluate the new scalar-limiting method, we performed three-dimensional simulations of temporal mixing layers with multiple species (as mentioned above). Here, the overshoots in species mass-fractions are mitigated without significantly affecting the growth of the mixing layer and Reynolds stresses. Finally, we investigated high-Reynolds number chemically reacting HF flows by performing large eddy simulations corresponding to the experiments of Slessor et al. (1998) at Caltech. Example results from this simulation are shown in Figure 26. The Q-criterion plot shows rich eddy content indicative of low levels of numerical dissipation.

Temperature profiles from the simulation, although close to the experimental results, do not show satisfactory agreement at present. Again, the computed temperature distribution is very sensitive to the specification of the inflow conditions. Further investigations are being conducted to address this issue, and will be the focus of research in the future.

We conclude this section by mentioning a topic that was explored but which is *not* part of the focus of the AFOSR-funded research, but one that benefitted from it and provides a rich testing and validation environment for these methods and considerations. In particular, an exploration of active scalar transport was performed by exploiting techniques and progress made as part of Sections 2.4.1 and 2.4.2 of this report, focusing on the consequences of subgrid-scale modeling and active scalar bound control in atmospheric dynamics. That work relies on progress and advances documented recently on flows where SGS stability corrections have proven necessary (Chung and Matheou 2014), was co-sponsored by the DOE grant mentioned earlier, published by Matheou, Chung, and Teixeira (2016), and listed in the reference list of this report but not as a publication sponsored by the AFOSR grant. It demonstrates the importance of observing scalar bounds, especially active-scalar bounds, as well as the benefits of improved SGS modeling.

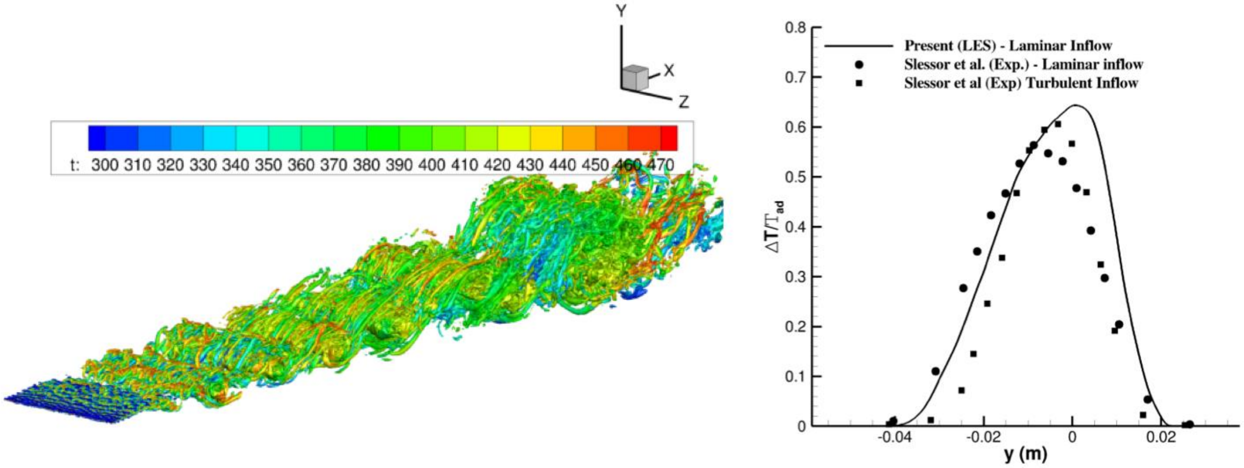

a)

b)

Figure 26. Three-dimensional reacting flow simulation a) Q-criterion plot and b) comparison of present temperature profile with experimental data.

2.5 Compressible and variable-density SGS modeling

Compressible and variable-density turbulence is described by non-linear partial differential equations that represent the conservation of mass, momentum, and energy. To derive the governing equations for large-eddy simulations, these equations are low-pass filtered on a space-time volume. Typically, this volume is related to the local grid element and has a characteristic dimension. The filtered variables become the solution variables, and there are unclosed terms in the governing equations due to filtering non-linear quantities. The effects of these subgrid-scale (SGS) terms cannot be resolved by the grid, and must be represented with a model.

Almost all CFD codes for variable-density flows rely on density-weighted (or Favre) filtering. The solution variables are, for example, $\tilde{u}_i = \overline{\rho u_i}/\bar{\rho}$, where the overbar represents the filtering operation, the tilde represents the Favre-filtered quantity, ρ is the density, and u_i is the velocity in the i direction. This simplifies the derivation of the filtered governing equations. However, it obscures the interaction between density variations and turbulent motion. For example, the filtered momentum flux in the i direction attributable to velocity in the j direction is $\overline{\rho u_i u_j}$, and its unresolved effects are modeled as $\tau_{ij} = \overline{\rho u_i u_j} - \bar{\rho}\tilde{u}_i\tilde{u}_j$, where $\bar{\rho}$, $\tilde{u}_i$, and $\tilde{u}_j$ are the resolved solution variables, and τ_{ij} is (here) the model for the unresolved subgrid-scale momentum flux.

The model must account for the difference between the filtered triple product of the density and velocity fields and the resolved momentum flux. This is a complicated quantity that embodies critical variable-density flow physics. However, its mathematical form provides no guidance as to how it should be represented in terms of the resolved-scale flow quantities.

Current LES models ignore the role of density variations in this product, and it is known that this approach cannot and does not capture the full dynamics of variable-density turbulence. Furthermore, filtering the energy equation results in a quadruple product for the unresolved kinetic energy flux; this term is also not modeled in existing CFD codes.

Under the present project, we derived an alternate mathematical form of the filtered governing equations for LES of variable-density turbulence (Sidharth, Kartha, and Candler 2016). These developments were based on prior studies of the effects of SGS baroclinic torque in the context of a variable-density extension to the SVM (GS, Candler, and Dimotakis 2014; GS and Candler 2015). The key idea is to apply unweighted filtering (or Reynolds-filtering), and then to use the transport equation for the subgrid-scale mass flux, $\overline{\rho u_i} - \bar{\rho}\overline{u_i}$, to eliminate terms. This results in a new form of the governing equations with several advantages:

- The governing equations are mathematically exact and represent the identical physics as the conventional Favre-filtered equations.
- The unresolved subgrid-scale terms involve only filtered double products, greatly clarifying the connection between the mathematical description and the turbulence.
- These terms can represent subgrid-scale counter-gradient diffusion and backscatter (small-scale motion driving motion at larger scales).
- There are terms for the subgrid-scale baroclinic torque (due to misalignment of density and pressure gradients) and acceleration (not represented in current LES models).
- The formulation is readily extensible to reacting flows and other complex variable-density turbulent flows.

The subgrid-scale terms are: the mass flux, specific stress, dilatational flux, pressure work, pressure acceleration, and internal energy flux. These terms are embedded in the Favre-filtered equations, but it is impossible to isolate them in the filtered triple and quadruple products.

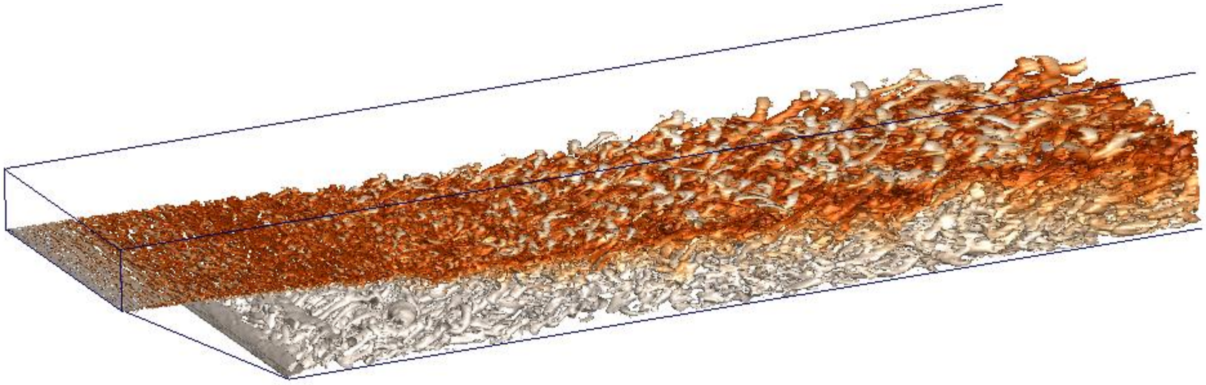

Figure 27. Filtered-velocity LES of a recirculating mixing layer: isosurface of Q criterion, colored by the chemical-product mass fraction. A gradient model was used for SGS pressure-acceleration modeling.

We have carried out direct numerical simulations of decaying variable-density turbulent flow to understand the effect of variable-density subgrid-scale terms. A budget analysis indicates that the new Reynolds-filtered subgrid-scale terms are non-negligible in the mean sense and their magnitude can locally exceed the magnitude of the conventional uniform-density stress term. The DNS cases are used to extract coefficients for a gradient-based SGS model. This new SGS model was applied to complex flows. For example, a recirculating mixing layer is simulated with the stretched-vortex model and this preliminary set of gradient model coefficients (the flow configuration and conditions correspond to the work of Bonanos et al. 2008). The LES results (Figure 27) are promising and are currently being further validated. A paper reporting on this approach is in preparation to be submitted for publication.

[This page intentionally left blank.]

3. Summary and conclusions

This report outlines and summarizes research progress and advances as a result of work under sponsorship of this Grant, as well as the co-sponsorship of some of the research topics by other funding, as outlined in Section 1.

In experimental work, the scaling of the delay length for initiation of chemical reactions downstream of the jet-injection station based on jet Reynolds number was established. This was confirmed to be dominated by turbulent mixing and not chemical-kinetic autoignition delay for the flows investigated. A 30^o jet inclination dramatically decreases jet-injection disturbances to the freestream, relative to normal-jet injection, but increases the distance to ignite, as a result of lower mixing rates. However, this penalty may be more than acceptable considering the (much) lower total-pressure losses as evidenced by the absence of (near-)normal shocks that normal injection generates. New experimental techniques were developed that allowed the non-intrusive measurement of convecting velocity fields, based on schlieren-imaging velocimetry (SICV). The techniques was used for a first validation of LES of jet-injection flow in a supersonic stream exploiting new geometric-optics modeling also developed as part of this grant. Small-scale experiments revealed the 3D and 4D behavior of scalar mixing providing guidance to subgrid-scale (SGS) modeling.

In large-scale direct-numerical simulations (DNS) turbulent behavior of the mixing of fluids with small to high density ratios subject to imposed acceleration fields revealed important new scaling of various statistics, also providing guidance for future subgrid-scale modeling of variable-density flows.

A new subgrid-scale combustion model was developed that also provides for efficient computation of complex chemical kinetics in a turbulent-mixing environment. Dubbed the evolution-variable manifold (EVM), it was integrated in a LES of turbulent combustion of a hydrogen jet in supersonic air crossflow, capturing many important flow features, perhaps for the first time. This modeling is best suited for capturing hydrocarbon combustion in the distributed-reaction zone (DRZ) regime but can also capture flame sheets with no changes in its structure.

The important topic of unphysical scalar excursions observed in finite-difference LES modeling received considerable attention. It was possible to attribute this behavior to dispersion errors of finite-difference operators. First attempts were made to mitigate these errors that must be controlled if passive and active scalar transport is to be simulated reliably and, in particular, if chemically reacting flows are to be reliably computed.

First attempts at variable-density and compressible-flow subgrid-scale model developments were made and preliminary simulations to assess their efficacy were made. However, this topic remains an open research challenge at this time.

A large number of presentations, conference papers, and publications derived from this effort, as listed in the Reference list in Section 5 of this report.

4. Personnel supported by this grant

Candler, Graham V. (Co-PI): McKnight Presidential Professor and Russell J. Penrose Professor, Associate Department Head, Aerospace Engineering and Mechanics, University of Minnesota

Cymbalist, Niccolo: Graduate Research Assistant, Aeronautics, California Institute of Technology. Ph.D. awarded in June 2016.

Dimotakis, Paul E. (PI): John K. Northrop Professor of Aeronautics and Professor of Applied Physics, California Institute of Technology.

Ferrero, Pietro: Graduate Research Assistant, Aerospace Engineering & Mechanics, University of Minnesota.

Gat, Ilana B.: Graduate Research Assistant, Aeronautics, California Institute of Technology.

Johnson, Heath: Senior Research Associate, Aerospace Engineering & Mechanics, University of Minnesota.

Kartha, Anand: Graduate Research Assistant, Aerospace Engineering & Mechanics, University of Minnesota

Lang, Daniel B.: Research Engineer in Aeronautics, California Institute of Technology.

Luthman, Elizabeth: Post-doctoral Research Fellow in Aeronautics, California Institute of Technology.

Matheou, Georgios: Visiting Associate in Aeronautics, California Institute of Technology, and Research Scientist, Jet Propulsion Laboratory.

Mehrotra, Prakhar: Graduate Research Assistant, Aeronautics, California Institute of Technology. Ae.Eng. awarded in June 2013.

Subbareddy, Pramod: Post-doctoral Researcher; now Assistant Professor, Mechanical and Aerospace Engineering, North Carolina State University

5. References

Ben-Yakar, A., M. Mungal, and R. Hanson 2006 Time evolution and mixing characteristics of hydrogen and ethylene transverse jets in supersonic crossflows. *Phys. Fluids* 18(2):026101; DOI: 10.1063/1.2139684

Bonanos, A.M., J.M. Bergthorson, and P.E. Dimotakis 2008 Mixing Measurements in a Supersonic Expansion-Ramp Combustor Flow," *Flow, Turbulence and Combustion* 80:489-506.

Burke, M.P., M. Chaos, Y. Ju, F.L. Dryer, and S.J. Klippenstein 2012 Comprehensive H_2/O_2 Kinetic Model for High-Pressure Combustion. *Int. J. Chem. Kinetics* 44:444-474.

Cabot, W.H., A.W. Cook, P.L. Miller, D.E. Laney, M.C. Miller, and H.R. Childs 2005 Large-eddy simulation of Rayleigh–Taylor instability. *Phys. Fluids* 17:091106-1, doi: 10.1063/1.1942519.

* Candler, G.V., N. Cymbalist, and P. Dimotakis 2015 Large-Eddy Simulation of Autoignition-Dominated Supersonic Combustion," AIAA-2015-3340.

* Candler, G.V., N. Cymbalist, and P. Dimotakis 2017 Wall-Modeled Large-Eddy Simulation of Autoignition-Dominated Supersonic Combustion. *AIAA J*. (to appear).

Chung, C. and G. Matheou 2014 Large-Eddy Simulation of Stratified Turbulence. Part I: A Vortex-Based Subgrid-Scale Model. *J. Atmospheric Sciences* 71:1863-1879; doi: 10.1175/JAS-D-13-0126.1

Chung, D., and D.I. Pullin 2010 Direct numerical simulation and large-eddy simulation of stationary buoyancy-driven turbulence. *Journal of Fluid Mechanics* 643:279–308; doi: 10.1017/S0022112009992801.

Cook, A.W., and P.E. Dimotakis 2001 Transition stages of Rayleigh-Taylor instability between miscible fluids. *J. Fluid Mech*. 443:69-99.

* Cymbalist, N., 2016 *Mixing, chemical reactions, and combustion in supersonic flows*. Ph.D. thesis, California Institute of Technology.

* Cymbalist, N., G.V. Candler, and P.E. Dimotakis 2016 Application of the Evolution-Variable Manifold Approach to Cavity-Stabilized Ethylene Combustion. AIAA Paper 2016-3481.

* Cymbalist, N., and P.E. Dimotakis 2015 On Autoignition-Dominated Supersonic Combustion," AIAA Paper 2015-2315.

* Cymbalist, N., D. Lang, E. Luthman, and P. Dimotakis 2017 A schlieren image-correlation velocimetry (SICV) technique for convective velocity estimates in high-speed turbulent flows. In preparation (to be submitted to *Experiments in Fluids*).

Dimotakis, P.E., 1986 Two-dimensional shear-layer entrainment. *AIAA J*. 24(11):1791-1796.

Dimotakis, P.E., 2000 The mixing transition in turbulent flows. *J. Fluid Mech*. 409:69–98.

* Ferrero, P., A. Kartha, P.K. Subbareddy, G.V. Candler, and P.E. Dimotakis 2013 LES of a High-Reynolds Number, Chemically Reacting Mixing Layer. AIAA Paper 2013-3185.

Gamba, M., and M.G. Mungal 2015 Ignition, Flame Structure and Near-Wall Burning in Transverse Hydrogen Jets in Supersonic Crossflow. *J. Fluid Mechanics* 780:226-273.

* Gat, I., G. Matheou, D. Chung, and P. Dimotakis 2016 Acceleration-driven variable-density turbulent flow. In proceedings, *VIIIth Int. Symp. on Stratified Flows* (San Diego, USA, 29 Aug. - 1 Sept. 2016).

* Gat, I., G. Matheou, D. Chung, and P. Dimotakis 2017 Incompressible variable-density turbulence subject to an external acceleration field. In preparation (to be submitted to *J. Fluid Mech.*).

Gruber, M., A. Nejad, T. Chen, and J. Dutton 1997 Large structure convection velocity measurements in compressible transverse injection flowfields. Experiments in Fluids

22(5):397–407, DOI 10.1007/s003480050066

* GS, Sidharth, A. Kartha and G.V. Candler 2016 Filtered Velocity Based LES of Mixing in High Speed Recirculating Shear Flow. AIAA Paper 2016-3184.

* GS, Sidharth, and G.V. Candler 2015 Stretched-Vortex Based Subgrid-Scale Modeling of Variable-Density Flows. AIAA Paper 2015-2782.

* GS, Sidharth, G.V. Candler, and P.E. Dimotakis 2014 Subgrid-Scale Modeling of Baroclinic Vorticity. AIAA Paper 2014-3214.

Jiang, G.S. and C.W. Shu 1996 Efficient Implementation of Weighted ENO Schemes. *Journal of Computational Physics* 126(1):202-228.

Jonassen, D., G. Settles, M. Tronosky 2006 Schlieren ‘PIV’ for turbulent flows. Optics and Lasers in Engineering 44(3):190–207; DOI: 10.1016/j.ast.2016.01.001

* Kartha, A., P.K. Subbareddy, G.V. Candler, and P.E. Dimotakis 2014 Large-Eddy Simulation of Supersonic Reacting Mixing Layers. AIAA Paper 2014-3030.

* Kartha, A., P. Subbareddy, G.V. Candler, and P. Dimotakis 2015 LES of Reacting Mixing Layers: Influence of Inflow Conditions and Heat Release. AIAA Paper 2015-3207.

Kida, S., and S.A. Orszag 1992 Energy and spectral dynamics in decaying compressible turbulence. *J. Sci. Comput*. 7(1):1-34.

Leonard, B.P., 1979 A stable and accurate convective modelling procedure based on quadratic upstream interpolation. *Computer Methods in Applied Mechanics and Engineering* 19(1):59–98.

* Luthman, E., N. Cymbalist, D. Lang, G. Candler, and P. Dimotakis 2017 Simulating schlieren and shadowgraph images from LES data. In preparation (to be submitted to *Experiments in Fluids*).

Matheou, G., D. Chung, and J. Teixeira 2016 On the synergy between numerics and subgrid scale modeling in LES of stratified flows: Grid convergence of a stratocumulus-topped boundary layer. In proceedings, *VIIIth Int. Symp. on Stratified Flows* (San Diego, USA, 29 Aug. - 1 Sept. 2016).

* Matheou, G., and P. Dimotakis 2014 Scalar excursions in large-eddy simulations. 7th AIAA Theoretical Fluid Mechanics Conference (AIAA Aviation and Aeronautics Forum and Exposition, June 2014, Atlanta, GA), AIAA Paper 2014-3209.

* Matheou, G., and P.E. Dimotakis 2016 Scalar excursions in large-eddy simulations. *Journal of Computational Physics* 327:97-120.

Morinishi, Y., T.S. Lund, O.V. Vasilyev and P. Moin 1998 Fully conservative higher order finite difference schemes for incompressible flow. *Journal of Computational Physics* 143(1):90-124.

Oevermann, M., 2000 Numerical Investigation of Turbulent Hydrogen Combustion in a SCRAMJET using Flamelet Modeling. *Aerospace Science and Technology* 4:463-480.

Papamoschou, D., 1989 A two-spark schlieren system for very-high velocity measurement. *Exp. Fluids* 7(5):354–356; DOI: 10.1007/BF00198454

Potturi, A.S., and J.R. Edwards 2015 Large-Eddy/Reynolds-Averaged Navier-Stokes Simulation of Cavity-Stabilized Ethylene Combustion. *Combustion and Flame* 162:1176-1192.

Saghafian, A., V.E. Terrapon, and H. Pitsch 2015 An Efficient Flamelet-Based Combustion Model for Compressible Flows. *Combustion and Flame* 162(3):652-667.

Slessor, M., C. Bond, C., and P.E. Dimotakis 1998 Turbulent Shear-Layer Mixing at High Reynolds Numbers: Effects of Inflow Conditions. *J. Fluid Mechanics* 376:115–138.

Smagorinsky J. 1963 General circulation experiments with the primitive equations. I. The basic experiment. *Mon. Weather Rev.* 91:99–164.

* Subbareddy, P.K., G.V. Candler, and P. Ferrero 2014 Scalar Conservation in Large Eddy Simulations of Reacting Flows. AIAA Paper 2014-3203.

Townsend, H., 1936 A method of air flow cinematography capable of quantitative analysis. *J. Aeronautical Sciences* 3(10):343–352; doi: 10.2514/8.267

Weirs, V.G. and G.V. Candler 1997 Optimization of weighted ENO schemes for DNS of compressible turbulence. *UMSI research report/University of Minnesota (Minneapolis, MN). Supercomputer institute* 97:177.

Note: References prepended with an asterisk denote publications of work funded, or co-funded, by this grant.

[This page intentionally left blank.]

AFOSR Deliverables Submission Survey

Response ID:7688 Data

1.

Report Type

Final Report

Primary Contact Email
Contact email if there is a problem with the report.

dimotakis@caltech.edu

Primary Contact Phone Number
Contact phone number if there is a problem with the report

626-395-4456

Organization / Institution name

California Institute of Technology

Grant/Contract Title
The full title of the funded effort.

Energy transformation, transfer, and release dynamics in high-speed turbulent flows

Grant/Contract Number
AFOSR assigned control number. It must begin with "FA9550" or "F49620" or "FA2386".

FA9550-12-1-0461

Principal Investigator Name
The full name of the principal investigator on the grant or contract.

Paul E. Dimotakis

Program Officer
The AFOSR Program Officer currently assigned to the award

Pauyl E. Dimotakis

Reporting Period Start Date

09/30/2012

Reporting Period End Date

11/30/2016

Abstract

Delay length for chemical-reaction initiation downstream of jet-injection was attributed to turbulent mixing and not chemical kinetics, for flows investigated. Inclined-jet injection dramatically decreases freestream-flow disturbances, relative to normal-jet injection, but increases ignition distance. This penalty may be acceptable considering the lower total-pressure losses than for normal injection. New experimental techniques developed allowed non-intrusive measurement of convecting velocity fields in supersonic flows and used for validation of LES of jet-injection flow in a supersonic stream. Small-scale experiments revealed 3D behavior of scalar mixing. In DNS, the turbulent fluid-mixing behavior of fluids with variable density revealed new scaling, providing guidance for subgrid-scale (SGS) modeling of variable-density flows. A new SGS combustion model (EVM) was developed for distributed-reaction zone (DRZ) environments allowing efficient computation of turbulent combustion, extending to hydrocarbon combustion. Integrated in a LES of turbulent combustion of a hydrogen jet in supersonic air

crossflow it captured many important flow features. Unphysical scalar excursions in finite-difference LES modeling were traced to dispersion errors of finite-difference operators. Many presentations, conference papers, and publications derived from this effort, as listed and discussed in the report.

Distribution Statement
This is block 12 on the SF298 form.

Distribution A - Approved for Public Release

Explanation for Distribution Statement
If this is not approved for public release, please provide a short explanation. E.g., contains proprietary information.

SF298 Form
Please attach your SF298 form. A blank SF298 can be found here. Please do not password protect or secure the PDF The maximum file size for an SF298 is 50MB.

AFOSR_FA9550-12-1-0461_Final_sf298_20170301b_1.pdf

Upload the Report Document. File must be a PDF. Please do not password protect or secure the PDF . The maximum file size for the Report Document is 50MB.

AFOSR_FA9550-12-1-0461_Final_20170301b.pdf

Upload a Report Document, if any. The maximum file size for the Report Document is 50MB.

Archival Publications (published) during reporting period:

Candler, G.V., N. Cymbalist, and P. Dimotakis 2015 Large-Eddy Simulation of Autoignition-Dominated Supersonic Combustion. AIAA-2015-3340.

Candler, G.V., N. Cymbalist, and P. Dimotakis 2017 Wall-Modeled Large-Eddy Simulation of Autoignition-Dominated Supersonic Combustion. AIAA J. (to appear).

Cymbalist, N., 2016 Mixing, chemical reactions, and combustion in supersonic flows. Ph.D. thesis, California Institute of Technology.

Cymbalist, N., G.V. Candler, and P.E. Dimotakis 2016 Application of the Evolution-Variable Manifold Approach to Cavity-Stabilized Ethylene Combustion. AIAA Paper 2016-3481.

Cymbalist, N., and P.E. Dimotakis 2015 On Autoignition-Dominated Supersonic Combustion," AIAA Paper 2015-2315.

Ferrero, P., A. Kartha, P.K. Subbareddy, G.V. Candler, and P.E. Dimotakis 2013 LES of a High-Reynolds Number, Chemically Reacting Mixing Layer. AIAA Paper 2013-3185.
Gat, I., G. Matheou, D. Chung, and P. Dimotakis 2016 Acceleration-driven variable-density turbulent flow. In proceedings, VIIIth Int. Symp. on Stratified Flows (San Diego, USA, 29 Aug. - 1 Sept. 2016).

GS, Sidharth, A. Kartha and G.V. Candler 2016 Filtered Velocity Based LES of Mixing in High Speed Recirculating Shear Flow. AIAA Paper 2016-3184.

GS, Sidharth, and G.V. Candler 2015 Stretched-Vortex Based Subgrid-Scale Modeling of Variable-Density Flows. AIAA Paper 2015-2782.

GS, Sidharth, G.V. Candler, and P.E. Dimotakis 2014 Subgrid-Scale Modeling of Baroclinic Vorticity. AIAA Paper 2014-3214.

Kartha, A., P.K. Subbareddy, G.V. Candler, and P.E. Dimotakis 2014 Large-Eddy Simulation of Supersonic Reacting Mixing Layers. AIAA Paper 2014-3030.

Kartha, A., P. Subbareddy, G.V. Candler, and P. Dimotakis 2015 LES of Reacting Mixing Layers: Influence of Inflow Conditions and Heat Release. AIAA Paper 2015-3207.

Matheou, G., and P. Dimotakis 2014 Scalar excursions in large-eddy simulations. 7th AIAA Theoretical Fluid Mechanics Conference (AIAA Aviation and Aeronautics Forum and Exposition, June 2014, Atlanta, GA), AIAA Paper 2014-3209.

Matheou, G., and P.E. Dimotakis 2016 Scalar excursions in large-eddy simulations. Journal of Computational Physics 327:97-120.

Subbareddy, P.K., G.V. Candler, and P. Ferrero 2014 Scalar Conservation in Large Eddy Simulations of Reacting Flows. AIAA Paper 2014-3203.

New discoveries, inventions, or patent disclosures:

Do you have any discoveries, inventions, or patent disclosures to report for this period?

No

Please describe and include any notable dates

Do you plan to pursue a claim for personal or organizational intellectual property?

Changes in research objectives (if any):

None

Change in AFOSR Program Officer, if any:

None

Extensions granted or milestones slipped, if any:

One-year no-cost extension

AFOSR LRIR Number

LRIR Title

Reporting Period

Laboratory Task Manager

Program Officer

Research Objectives

Technical Summary

Funding Summary by Cost Category (by FY, $K)

	Starting FY	FY+1	FY+2
Salary			
Equipment/Facilities			
Supplies			
Total			

Report Document

Report Document - Text Analysis

Report Document - Text Analysis

Appendix Documents

2. Thank You

E-mail user

Mar 01, 2017 13:13:21 Success: Email Sent to: dimotakis@caltech.edu